Nanoscale Advances

REVIEW

View Article Online
View Journal | View Issue

Cite this: *Nanoscale Adv.*, 2025, **7**, 6373

Self-organization of photonic structures in colloidal crystals in the AI era

Neha Yadav, Mingming Liu, Yongling Wu, Ashish Yadav * and Hongyu Zheng *

The advent of smart-engineered photonic materials, a development primarily influenced by the cutting-edge technology of artificial intelligence (AI), has ushered in a new era of unprecedented control over the manipulation and propagation of light. AI has been a driving force in the evolution of smart-engineered photonic materials, pushing the boundaries of what was once thought possible. Over the past few decades, using rationally engineered photonic structures for the unconventional control of light has become one of the most exciting frontiers in photonics and materials science. These artificially structured optical media, which include photonic crystals, plasmonic components, and optical metamaterials, have led to transformative changes in the entire vistas of optics science. Photonic crystals (PhCs) have gained significant attention from researchers due to their ability to self-assemble. PhCs exhibit physical properties such as photonic bandgaps, high reflectance/transmittance, low loss, and lasing in the visible range of wavelengths needed for optical systems of desired performance. For the application of these properties, significant efforts are being made to explore novel, cost-effective fabrication methods to develop 3D-PhCs based on nanoscience and nanotechnology, with AI playing a pivotal role. Nano-PhCs have enhanced optical and lasing properties, resulting in miniaturized optoelectronic systems with higher measurement reliability than existing systems. Keeping such advancements in view, this review discusses the latest techniques explored in AI technology to fabricate nano-PhCs, the specific role of AI in the fabrication process, and, notably, their potential applications in energy harvesting and artificial intelligence.

Received 6th May 2025
Accepted 9th July 2025

DOI: 10.1039/d5na00449g

rsc.li/nanoscale-advances

Center for Advanced Laser Manufacturing (CALM), Shandong University of Technology, Zibo, 255000, P. R. China. E-mail: zhenghongyu@sdut.edu.cn; ashish@sdut.edu.cn

Neha Yadav

Dr Neha Yadav obtained her Bachelor's degree in Science and Master's degree in Computer Applications. Now she is pursuing a PhD degree at the Center for Advanced Laser Manufacturing (CALM), and she is working on innovative materials and artificial intelligence sensors.

Yongling Wu

*Yongling Wu received BEng. and MEng. degrees in mechanical engineering from Tsinghua University, Beijing, China, in 1985 and 1988, respectively, and a PhD degree in materials science and engineering from Nanyang Technological University, Singapore, in 2009. She is currently a Professor at Shandong University of Technology, Zibo, China. She is a Senior Scientist at the Agency for Science, Technology and Research (A*STAR), Singapore, and the Group Manager of the Surface Technology Group. Her team received the National Technology Award of Singapore. Her research areas cover nanomaterials and coatings, surface science and engineering, multifunctional composite materials, laser materials processing, and flexible wearable sensors. Dr Wu is a Standing Member of Chinese Surface Engineering Society.*

1. Introduction

Modeling has been a key element in designing, controlling, and optimizing processes for several years.[1,2] It serves as a fundamental engineering tool. However, creating a model demands in-depth knowledge of the underlying process mechanisms, which can considerably lengthen the development timeline.[3–5] Recently, engineers have integrated modeling with simulations and experiments, utilizing large datasets to enhance prediction accuracy from experimental data. Among various modeling approaches, artificial intelligence (AI) algorithms that emulate human intelligence or actions are especially effective for managing extensive datasets.[6] Machine learning (ML), a subset of AI, enables machines to learn from user interactions and data inputs, facilitating automatic evaluation and responses in real-world production environments. This approach supports human problem-solving, minimizes errors, boosts efficiency, and draws on fields such as probability theory, statistics, approximation theory, and complex algorithms. This AI-driven method has applications across diverse domains, including photonics, neuroscience, computer science, statistics, social sciences, chemistry, and robotics. Photonics is defined[7–9] as the science and engineering of light–matter interactions that take place on wavelength and subwavelength scales where the physical, chemical, or structural nature of natural or artificial nanostructure matter controls the interactions, so it is also called nanophotonics. Over the next ten years, nanophotonic structures and devices promise dramatic reductions in the energy of device operation, densely integrated information systems with lower power dissipation, enhanced spatial resolution for imaging and patterning, and new sensors with increased sensitivity and specificity. Nanophotonics concerns investigations into building, manipulating, and characterizing optically active nanostructures to create new capabilities in instrumentation at the nanoscale, chemical and biomedical sensing, information and communications technologies, enhanced solar cells and lighting, disease treatment, environmental remediation, and many other applications.

The rapid development of artificial intelligence (AI) has made inverse design ideas a reality. As part of AI, the main optimization algorithms include simulated annealing,[9] genetic algorithm,[10] particle swarm optimization,[11] and topology optimization.[12–15] These mature algorithms have been widely reported for achieving on-demand inverse designs. They usually rely on the intermediate results obtained by iterative forward design schemes. Due to the limitations of an entirely random search, completing the inverse design under multiple constraints remains a significant challenge. Since the 1980s, machine learning (ML) has gradually become a dominant paradigm in the AI community.[16,17] The basic unit of the artificial neural network, the M–P neuron, was proposed in 1943.[18] In 1949, Hebb's rule was proposed, suggesting that the basis of neuron learning and memory lies in the variable connection strength between neurons.[19] In 1958, Rosenblatt[20] proposed the perceptron model, which gave the learning mechanism of neural networks for the first time.[21] However, this model does not contain hidden layers and can only handle linearly separable problems. Multilayer neural networks (MNNs) were significantly improved by the proposal of a back-propagation algorithm for neural network training in the 1980s.[22] However, they remained limited by the amount of data and computing power. In the new century, deep learning technology experienced rapid growth after 2006,[23,24] and a series of algorithms were derived from deepening the structure of artificial neural network models, also known as deep neural

Ashish Yadav

Ashish Yadav, PhD, is an Assc. Professor at Shandong University of Technology, China. He received a PhD degree from the Department of Physics at the University of Roma Tor Vergata, Italy, in 2014. His work focuses on advanced self-assembly-based photonic crystals and plasmonic nanostructures. Presently, he is working on fabrication methods and the development of three-dimensionally ordered high-quality photonic crystal films and their application as optical materials for lasing and devices. He is working in multi-directional research, e.g., wearable electronics, sensors, and energy harvesting devices, and is also interested in laser spectroscopy techniques for low-threshold devices and ultrafast laser–matter interactions.

Hongyu Zheng

Hongyu Zheng is a Professor and the dean of School of Mechanical Engineering, Shandong University of Technology. He obtained his BEng in Mechanical Engineering from Tsinghua University in 1985, and PhD in Laser Materials Processing from Imperial College London in 1990. Prior to joining Shandong University of Technology (SDUT), he was a principal scientist at the Agency for Science, Technology and Research (A-STAR) of Singapore leading a research team in laser materials processing. Prof. Zheng has co-authored more than 300 journal papers. In 2014, he and his team were awarded the IES Prestigious Engineering Achievement Award of Singapore. Prof. Zheng has been an elected Fellow of the International Society of Nano-Manufacturing (ISNM) since 2014. His current research interests include ultrafast laser–matter interactions, micro-/nano-processing mechanisms, in-process monitoring and data analytics.

networks (DNN). This was supported by the development of big data science and improved computer performance that provided hardware support. Meanwhile, the development of open-source and flexible software platforms, such as TensorFlow,[25] PyTorch,[26] and Keras,[27] made it easy for beginners to build generic deep architectures. The third wave of AI started to bring profound industrial changes in various aspects of modern society, such as computer vision,[28] natural language processing,[29] speech recognition,[30] AlphaGo,[31] robotic controls,[32] *etc.* As one of the most essential branches of machine learning, deep learning has become the fundamental route in complex hierarchical feature learning.

1.1. Basic concepts of photonic crystals

These three types of PCs require different fabrication methods (Fig. 1):

1-D PCs are alternating dielectric layers deposited or adhered to a substrate. For instance, this type of PC can be fabricated by programmed deposition techniques such as evaporation, sputtering, epitaxial growth, or lithography. An example is the Bragg reflector.

2-D PCs presented a periodicity in two spatial directions, while in the third direction, the crystal is homogeneous. Such a structure can be realized, for example, by fabricating a lattice of dielectric columns or drilling a lattice of pores into a dielectric material. This kind of structure is usually manufactured using lithographic techniques.

3-D PCs require a periodic refractive index variation in three spatial directions. This type of structure is the most difficult to realize, and the top-down approaches of deposition and lithographic techniques are not well suited for fabricating this type of PC. So far, the most promising approach to fabricating a 3-D PC is colloidal self-assembly in which small dielectric spheres suspended in a fluid automatically arrange themselves into close-packed face-centered cubic crystals by surface forces (bottom-up processing). This kind of crystal is called a colloidal photonic crystal. Moreover, examples of 3-D PCs are natural materials like opals, butterfly wings, and peacock feathers.[33]

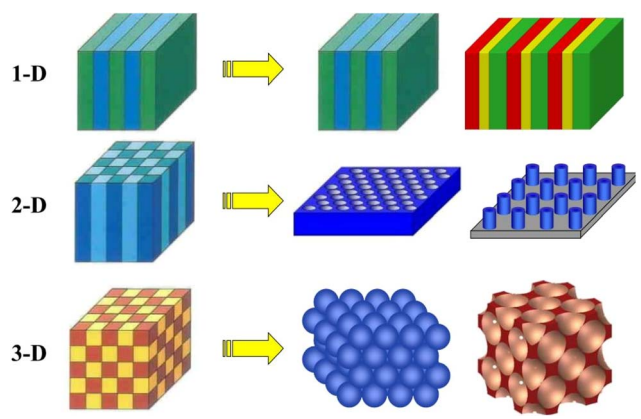

Fig. 1 Schematic representation of a 1-D, 2-D and 3-D PC. Different dielectric materials are shown in different colors.[1,2]

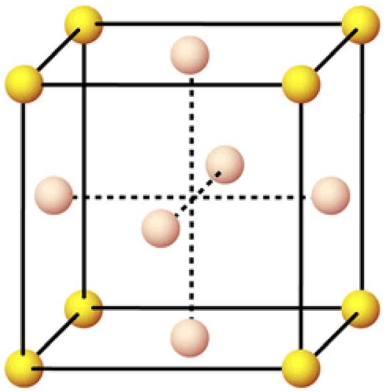

Fig. 2 FCC crystal structure.

This thesis focuses on three-dimensional colloidal photonic crystals. As mentioned, the CPCs are composed of spheres that assemble spontaneously into an FCC lattice, similar to the arrangement of atoms in a sodium chloride (NaCl) crystal. This lattice belongs to the cubic system. The atoms are arranged at the corners and center of each crystal unit cell's cube face. The FCC crystal structure is shown in Fig. 2. This preferential configuration is the lowest energy configuration for the packing of hard spheres, as it maximizes the filling factor (f), which is the ratio of the volume occupied by the spheres to the total volume of the crystal. An ideal FCC lattice has a filling factor of 0.74. PCs with different crystalline structures can also be fabricated, resulting in a different filling factor value.

Other relevant features of photonic crystals are the photonic band gap or stop band, which is a range of wavelengths that cannot propagate into the PC structure in analogy to the energy gap for the electrons in a solid and the dielectric contrast, which is the ratio between the highest and the lowest index of refraction of the two materials which compose the structure. The stop band and the dielectric contrast are related to each other. A high dielectric contrast is vital since stop bands appear above a certain dielectric contrast threshold for a given crystal structure. Then, they increase nearly monotonically in width with the dielectric contrast.

The optical properties of PCs, particularly the scattering of light on a photonic crystal structure, can be described using different approaches. A simple description is the Bragg picture, developed initially to describe the scattering of X-rays on electronic crystals. This description is also suitable for light scattering on a photonic crystal. It allows for obtaining relevant information on PCs, such as the stop band position. More information can be obtained using traditional solid-state physics approaches to calculate the complete PC band structure. The following paragraphs will provide a brief discussion of the theory of Bragg diffraction of light in PCs and the calculation of the PC band structure.

1.2. Bragg diffraction of light in photonic crystals

The behaviour of PCs in interaction with an electromagnetic wave can be described using a simple Bragg approach. The

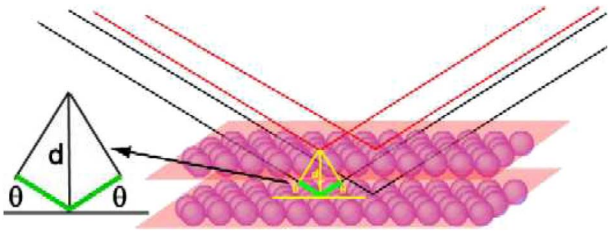

Fig. 3 Conditions for the Bragg diffraction of light on a PC structure: constructive interference between adjacent crystal planes.[35]

diffraction of light depends on the crystal structure and the wavelength of light. When the wavelength is greater than the lattice constant (the distance between two crystal planes), ordinary refraction of light occurs. Diffraction occurs when the wavelength is comparable to or smaller than the lattice constant. The diffracted beams are found in directions quite different from the incident direction. W. L. Bragg explained this phenomenon: the incident waves are reflected specularly from parallel crystal planes, with each plane reflecting just a small fraction of the incident light. In specular reflection, the angle of incidence is equal to the angle of reflection. The diffracted beams are found when parallel plane reflections interfere constructively.[34] The same description that Bragg used for X-rays on atomic crystals can be applied to the description of the diffraction of light on a photonic crystal structure as shown in Fig. 3.

The diffraction of light is achieved from the scattering and interference produced by coherent waves in periodic PC structures. In particular, in the case of 3-D CPCs, the periodic arrays of spherical particles provide a periodic structure that acts as a diffraction grating for light waves, particularly when the lattice constant is of the same order of magnitude or smaller than the wavelength of the incident light. This means that the wavelength range in which Bragg diffraction of light is observed depends on the size of the spheres.

Considering parallel lattice planes spaced by d_{hkl}, the interplanar spacing between the scattering planes, the interplanar spacing d_{hkl} for (hkl) planes in the FCC lattice can be calculated using the following relation.

$$d_{hkl} = \frac{a}{\sqrt{(h^2 + k^2 + l^2)}}$$

where a is the unit cell size, the notable (hkl) sets of the diffraction planes that strongly participate in light diffraction of an FCC type lattice are (111), (220) and (200); the focus will be on the (111) set of planes because it is the most densely packed.

The path difference for rays reflected from adjacent planes is $2d_{hkl}\cos\theta_{int}$, where θ_{int} is the internal angle (see Fig. 3). It is evident from the figure that $\theta = 90° - \theta_{int}$. Constructive interference from successive planes occurs when the path distance is an integer number m of wavelength λ. This formula thus represents the Bragg condition:

$$m\lambda = 2d_{hkl}\cos\theta_{int}$$

where m is the diffraction order ($m = 1, 2, 3\ldots$), λ is the free space wavelength of light, d_{hkl} is the interplanar spacing between the scattering planes (labeled by the Miller indices), and θ_{int} is the internal angle.

Considering a flat interface between two dielectrics with different refractive indices (n_1 and n_2), light can be described by a ray with an incident angle θ_{int} and a refracted angle θ_{ext} given by Snell's law. The external incidence angle on the sample is controlled in the experimental measurements.

$$n_1 \sin\theta_{int} = n_2 \sin\theta_{ext}$$

The indices refer to the external and internal refractive indices and angles. The resulting modified form of Bragg's law for the optical region that takes into account Snell's law of refraction is:

$$m\lambda = 2d_{hkl}\sqrt{(n_{eff}^2 - \sin^2\theta_{ext})}$$

where n_{eff} is the effective refractive index of the PC; for calculating the effective refractive index, among the approximated expressions proposed for the bulk dielectric properties of inhomogeneous materials, the simplest ones are the mixing rules, based on the additive property:

$$n_{eff}^2 = f n_1^2 + (1 - f) n_2^2$$

This form of Bragg's law allows one to know the gap position in first approximation because it represents the longest wavelength diffracted by the PC for an observer perpendicular to the surface. This approach can be applied only to systems with moderate dielectric contrast; therefore, it is a well-suited technique for studying polymeric CPCs.

1.3. Photonic band structure

A PC is a medium with a periodic modulation of the dielectric constant. This results in interesting differences in the optical properties of a homogeneous medium. First, a photonic crystal exhibits a band structure similar to that of an electronic crystal. The band structure represents the relationship between the energy and the propagation direction of the radiation inside the crystal. It is a tool to predict and study the photonic answer of our system, as it permits one to know the allowable energy levels for the photons. To understand this concept, a comparison between the similarities in the behavior of photons therein and electrons in solids has to be made, using some ideas of solid-state physics. An electronic crystal can be viewed as a periodic distribution of basic units, such as atoms or molecules, which scatter in the periodic lattice; as a direct consequence of this periodicity in the electronic potential, the energy levels are eventually restricted to certain allowed energy bands separated by energy gaps.

In a PC, the photons scatter in the periodic lattice similarly and present bands and gaps for photon states. The Schrödinger equation for an electron of effective mass m in a crystal, in which the potential is $V(r)$, can be written as:

$$\left[-\frac{\hbar}{2m}\nabla^2 + V(r)\right]\Psi(r) = E\Psi(r)$$

where $V(r)$ is a periodic function with the periodicity of the lattice, R: $V(r) = V(r + R)$. The eigenstates of this equation are also periodic functions with period R. The dispersion relationship derived, $E(k)$, will present a forbidden band for all energies E with imaginary values. Similarly, in a medium where a spatial modulation of the dielectric constant $\varepsilon(r)$ exists, photon propagation is governed by the classical wave equation. Maxwell's equations can be treated as an eigenproblem, in analogy with Schrödinger's equation. It can be expressed in terms of the magnetic field $H(r)$ as:

$$\nabla \times \left[\frac{1}{\varepsilon(r)}\nabla \times H(r)\right] = \left(\frac{\omega}{c}\right)^2 H(r)$$

where $\varepsilon(r)$ is the dielectric function and c is the speed of light. This is an eigenvalue equation, with eigenvalue ω/c. In a PC, $\varepsilon(r)$ is a periodic function: $\varepsilon(r) = \varepsilon(r + R)$.

The electron wave equation provides the band diagram by utilizing electron standing waves, which represent the allowed energies (bands) and the forbidden energies (band gaps). The photon wave equation lets us know the' permitted and forbidden frequencies of photons.

It is essential to note that while the electron wave equation is not scalable, since an intrinsic length measure is associated with the electron—the de Broglie wavelength—the photon wave equation is scalable instead. Suppose a PC presents a given periodicity length. In that case, it will display photonic bands within a specific frequency range, and scaling it will result in a new system with precisely the same band scheme, only scaled accordingly. If we halve the size, we double the energy.

The equation can be solved by using the Bloch approach: the eigenfunctions may be written as the product of a plane wave envelope function e^{ikx} and a periodic function (Bloch function) $H_{nk}(x)$ that has the same periodicity as the dielectric lattice, with eigenvalues $\omega_n(k)$, $H(x) = e^{ikx}H_{nk}(x)$. The periodic function $H_{nk}(x)$ satisfies:

$$(\nabla + ik) \times \left[\frac{1}{\varepsilon}(\nabla + ik) \times H_{nk}\right] = \left(\frac{\omega_n(k)}{c}\right)^2 H_{nk}$$

yielding a different Hermitian eigenproblem over the primitive cell of the lattice at each Bloch wavevector k. This primitive cell is a finite domain if the structure is periodic in all directions, resulting in discrete eigenvalues ($n = 1, 2, \ldots$). These eigenvalues, $\omega n(k)$, are continuous functions of k, forming discrete bands in a band structure or dispersion diagram when plotted against k.

In such a diagram, the energy eigenvalues are separated in energy by a finite spacing at each k. When the separation extends over all wave vectors, it is referred to as a band gap.

Due to this periodicity, one needs only to compute the eigen solutions for $n = 1$ within the primitive cell of this reciprocal lattice or, more conventionally, one considers the set of inequivalent wavevectors closest to the $k = 0$ origin, within a region called the first Brillouin zone.

The calculation of the complete band structure of a PC allows one to know the exact location and size of the photonic band gaps for a given PC structure, and thus it is a crucial predictive tool in PC design. Fig. 4 shows two examples of photonic band structures calculated for the 1D and 3D structures plotted in the exact figure. The most noticeable feature in both band diagrams is the existence of frequencies, where no modes are available in the direction of periodicity. Such regions are known as photonic band gaps (PBGs) and represent the primary feature of PCs. Light propagation within the sample is not allowed for the frequencies within this spectral range. In the top panel (Fig. 4(a)), a 1-D photonic crystal is sketched. The dielectric function is modulated only in the z direction; thus, light propagation can be inhibited only in this direction. For light propagating along the x and y directions, the 1-D PC acts as a homogeneous medium. Such a configuration is exploited, for instance, in the distributed Bragg reflector (DBR), which will be illustrated in the following paragraph.

In a 3-D PC like the FCC colloidal crystal made of dielectric hard spheres sketched in Fig. 4(b), the light propagation can be inhibited in all the spatial directions, leading to interesting new physical phenomena.

Properly engineered PBGs may control the photonic density of states (DOS) – the number of states per unit of energy. In particular, when an emitter such as a dye is embedded into the PC, the PBG can inhibit the emitter's spontaneous emission.[37] The Fermi golden rule governs the spontaneous emission process, which is a method for calculating the transition rate (probability of transition per unit time) from one energy eigenstate of a quantum system to a continuum of energy eigenstates, due to a perturbation. We consider the system to begin in an eigenstate, Ψ_i, of a given Hamiltonian, H_0. Then, we believe the effect of a (possibly time-dependent) perturbing Hamiltonian, H'. If H' is time-independent, the system goes only into those states in the continuum that have the same energy as the initial state. If H' oscillates as a function of time with an angular frequency ω, the transition is into states with energies that differ by $\hbar\omega$ from the energy of the initial state. In both cases, the one-to-many transition probability per unit of time from the state Ψ_i to a set of final states Ψ_f is given, to first order in the perturbation, by:

$$T_{i\to f} = \frac{2\pi}{\hbar}|M_{fi}|^2\rho$$

where ρ is the density of final states and M_{fi} is the matrix element (in bra-ket notation) of the perturbation H' between the final and initial states:

$$M_{fi} = \langle\Psi_i|H'|\Psi_f\rangle.$$

An emitter embedded into a PC finds a zero density of final states in the band gap energy range. No final states are available for the emission in such an energy range, and the emitter must remain excited. This is suppression of the spontaneous emission. In a PC, ρ and M_{fi} can be engineered appropriately also to enhance the emission. Typically, a higher density of states is obtained at the edges of a PBG, resulting in enhanced emission.

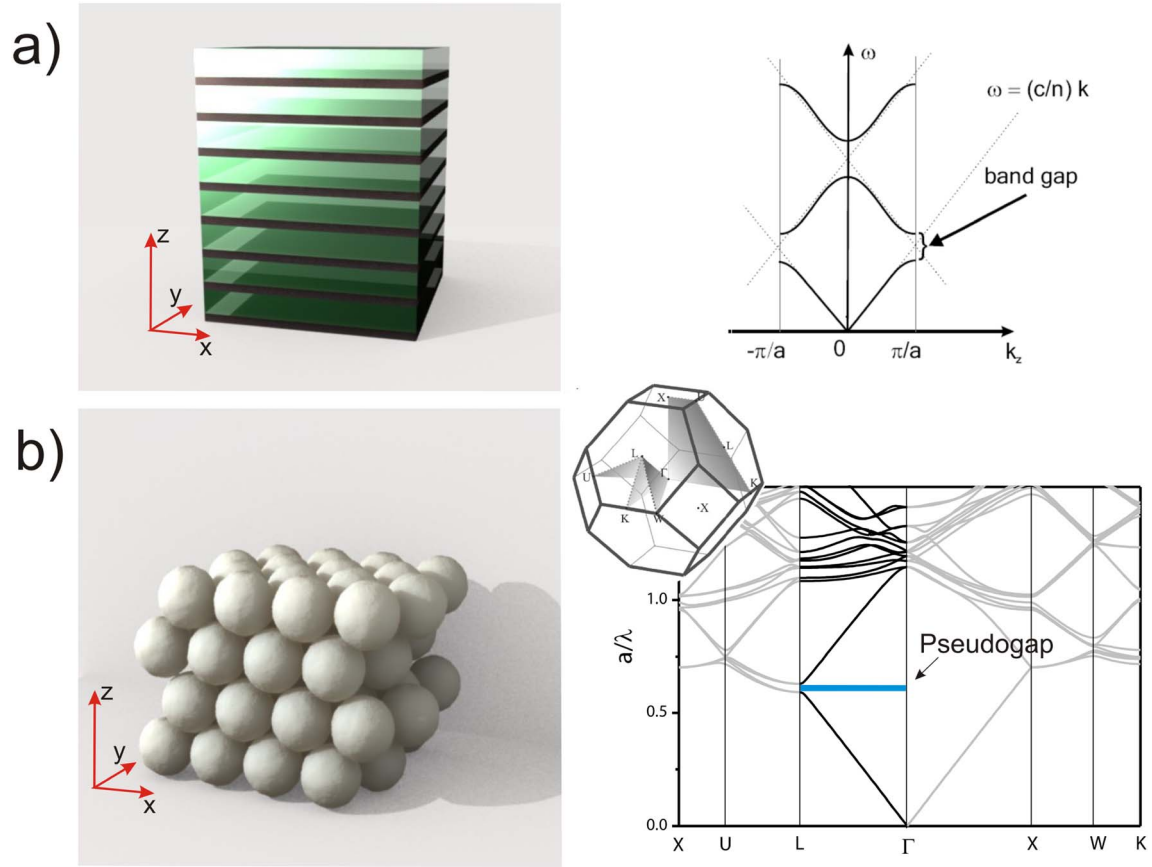

Fig. 4 (a) 1D PC structure (left) and dispersion relation for light propagating along the *z* direction (right). (b) 3D CPC structure (left) and dispersion relation along the high symmetry directions of the crystal structure (right).[36]

This can be exploited to observe amplified spontaneous (ASE) and laser emission.

Another possibility to achieve control of the light in the PC is to create defects. Like in a semiconductor material, a defect results in a state in the gap of the material, which is also localized in space. In a PC, the electromagnetic (EM) field mode in the gap will remain spatially confined in the vicinity of such a defect since its propagation in the material is forbidden. Such a defect acts as a resonant cavity for the EM field. The magnitude describing the confining power of the cavity is called the quality factor Q, which measures the rate of escape from the cavity. The quality factor is defined as:

$$Q = \frac{\Delta\omega}{\omega}$$

where ω is the frequency of the transition and $\Delta\omega$ is the width of the resonance. High Q cavity is promising for low threshold lasers since they make better use of the pump energy, but a compromise is necessary to allow efficient light extraction.

2. Methods of photonic crystal synthesis & fabrication

The theory of PhCs has been extensively studied over several years, and many phenomena are predicted by using PhCs in the visible and near-IR wavelength regions. Still, the experimental realization of these crystal structures is not easy and faces several fabrication difficulties. Current micro- and nano-fabrication techniques struggle to achieve this order of magnitude of spatial modulation of refractive index in all three orthogonal directions. In design, the method used for the fabrication should be easy to implement, have a low cost, and give reproducible results. First, some essential techniques for fabricating 1D, 2D, and 3D-ordered PhCs are briefly summarized. The 1D PhCs are well-known for their multilayer structure. Various methods, including evaporation techniques, sputtering, and dip-spin coating,[28] are employed for fabricating 1D PhCs. Anodic etching of crystalline silicon is another method for creating 1D PhCs. These crystals are also manufactured using low-pressure chemical vapor deposition.[29] Fabrication conditions can be modified to introduce defects in these structures.

The fabrication of 2D PhCs uses techniques adopted from the microelectronics industry. A 2D structure with the bandgap in the near IR wavelength region can be fabricated using the technology for preparing microchannel plates.[30–32] A modified form of this technique is used to create 2D PhCs in the visible and ultraviolet wavelength regions.[38] Photolithography and electron beam lithography are also extensively used to make 2D PhCs.[39] These methods also create waveguides and point

defects in these 2D PhCs.[40] Fabrication of 3D PhCs is quite challenging compared to 1D or 2D PhCs. Lithography techniques, such as photolithography and electron beam lithography, enable the fabrication of 3D-ordered PhCs. These techniques depend upon whether the optical or electron beams are used to write the pattern on a base material. Two methods, designed by Noda *et al.*[41] and Lin *et al.*,[42] are used for fabricating 3D PhCs.

These structures are commonly referred to as woodpiles or layer-by-layer structures. 3D PhCs with a complete bandgap are fabricated using this lithography technique.[43–45] Another technique that has been widely used is the holographic technique. The basis of this method is the interference of four non-coplanar laser beams within a photo-inductive material to create a periodic structure whose period and symmetry can be controlled. Compared with the above methods, a simple and inexpensive method for fabricating 3D PhCs is based on the self-assembly of microparticles in a colloidal suspension. The first structure fabricated using the polystyrene colloidal suspension is by Velev *et al.*[46] Similar structures have been manufactured using silica colloidal suspensions.[47,48]

A variety of self-assembling methods are used for making PhCs. Depending on the force involved in assembling microparticles, the self-assembling technique can be classified into three categories: (1) gravitational self-assembly,[49,50] (2) convective self-assembly,[51–53] and (3) inward-growing self-assembly.[54,55] All these methods have certain advantages and disadvantages. Self-assembling methods are pretty inexpensive and do not require sophisticated laboratory equipment. Another area where the PhCs can have a significant impact is designing photonic devices based on nonlinear optical characteristics in these structures,[56–60] where the PhCs are made of materials that have substantial nonlinear effects and while the incident light is at the band edge wavelength, nonlinear optical processes such as harmonic generation can be enhanced.[61] The application of PhCs, having been successfully commercialized to date, is in the form of PhC fibers. In these fibers, light guidance is achieved through the bandgap effect rather than total internal reflection. This is achieved by surrounding a hollow core with an air core, resulting in very low propagation losses. The minimization of nonlinear optical effects and single-mode operation over an infinite range of wavelengths make these fibers attractive for various applications.

Fabrication of 1D or 2D PBG crystals is relatively straightforward. For example, 1D systems can be easily generated through the programmed deposition of alternating layers of different dielectric materials.[62,63] In contrast, 2D systems can be routinely produced *via* the selective etching of the underlying substrates using masks.[64] As a result, 1D and 2D PhCs have been widely used in fabricating a rich variety of commercial devices, such as optical notch filters,[65] dielectric mirrors or optical resonance cavities,[66] and Bragg gratings (on optical fibers).[67] At the current stage of development, it remains a significant challenge to apply conventional patterning techniques to the generation of pre-designed, 3D periodic lattices that will meet all the criteria required for creating complete photonic band gaps.[68] Some relatively simple 3D mesostructures amenable to layer-by-layer patterning have recently been fabricated in the prototype form by several research groups and were shown to exhibit the signature of complete band gaps down to the near-infrared region.[69,70] Some processing difficulties limited the formation of such 3D periodic structures only up to some layers (less than 10). Besides, the materials used are not those commonly used in microelectronic engineering.

Since the position of a photonic bandgap is often scaled by half to one-third of the periodicity of a 3D lattice, the fabrication task is expected to become more challenging as the bandgaps move towards the visible or ultraviolet regions. In these regions, one will need to pattern the dielectric materials into microstructures of 100 ± 300 nm in size along all three dimensions and to accomplish registration among these structures in different layers with an accuracy of better than tens of nanometers. These technical challenges to extending conventional microlithographic techniques to 3D patterning have led scientists and engineers to consider alternative approaches.[57] Notable examples actively explored in this regard include laser-guided stereolithography,[71] two-photon-induced deposition or polymerization,[72] 3D holographic patterning with multiple laser beams,[73] and self-assembly.[74] At present, the feature sizes that could be routinely achieved using the first two methods are still on the order of a few micrometers due to optical focusing problems and diffraction effects, and the holographic method has been shown to have a relatively high requirement on the experimental setup, including the exposure and development of photosensitive materials. Among all alternative methods for 3D patterning, self-assembly seems to be the most promising approach to the cost-effective production of 3D periodic structures.

The self-assembly of latex particles is a complex interaction process involving gravity, electrostatic repulsion, and Brownian motion.[75] Nagayama and his coworkers[76,77] first demonstrated that the assembly of latex particles is primarily driven by capillary force and convective interaction. The capillary force between latex particles organizes the particles into a hexagonal 2D array on a flat substrate. Fig. 5(a) and (b) schematically illustrate the latex arrangement formation process. At first, a nucleus was formed when the thickness of the liquid layer approached the diameter of the particles. Then, convective transport drove more particles toward this nucleus, creating a 2D hexagonal latex array based on the attractive capillary force. In this process, both temperature and humidity[78] are crucial for the convective force and the rate of assembly, and the latter is also affected by electrostatic repulsion between the latex particles.[79,80] Additionally, the gravitational force will hinder the assembly of larger particles. Various assembly approaches have been developed based on these assembly forces to control the assembly of latex particles.

The self-assembling strategy involves depositing latex particles through vertical deposition.[83,84] A simplified convective assembly process is achieved by putting a vertical glass substrate into the latex suspension, which is pulled upward slowly, as shown in Fig. 5. The latex particles would be transferred by capillary force to the glass substrate during evaporation, that is, solvent evaporation causes a convective particle

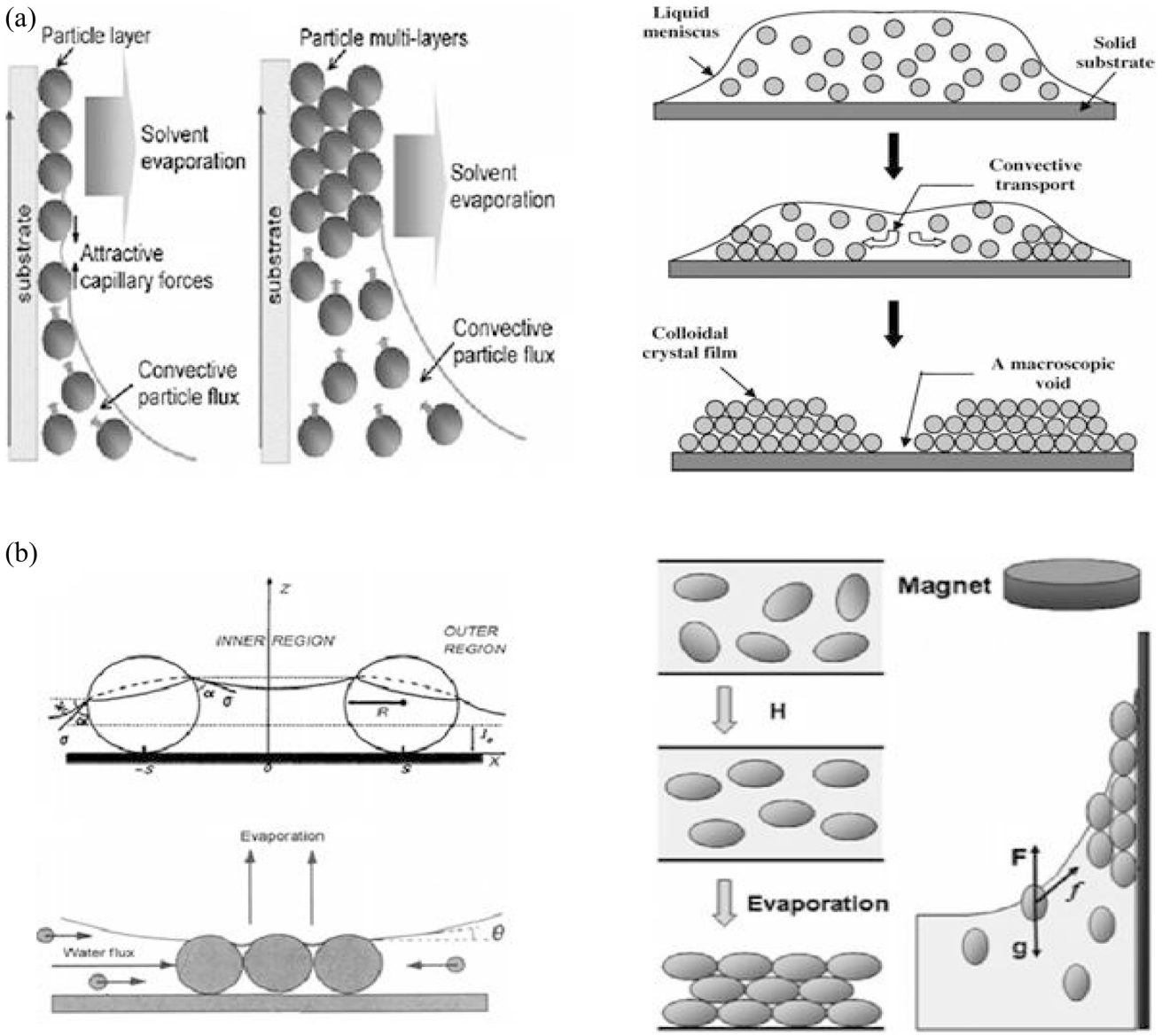

Fig. 5 The self-assembly of colloidal particles in the vertical deposition technique for (a) single- and (b) multi-layer colloidal crystals.[81] Schematic representation of the inward-growing self-assembly mechanism for colloidal crystal films deposited on a horizontal solid substrate.[18] Schematic illustrations for the self-assembly of latex particles driven by liquid flow on a horizontal hydrophilic substrate: nucleus formation and crystal growth.[76,77] Schematic illustration for latex particle assembly under a magnetic field.[82]

flux from the bulk of the colloidal suspension toward the drying particle layer. The balance between capillary force and convective particle flux during solvent evaporation is essential for forming 2D and 3D colloidal crystals. In this process, the crystal thickness could be well controlled by the latex suspension concentration or particle diameter concentration, as shown in Fig. 5.[81]

2.1. Horizontal deposition of colloidal crystal films

Now, let's look at the self-assembly mechanism of colloidal particles confined in a concave aqueous layer. The growth of the colloidal crystal film was observed to originate from the middle of the aqueous layer. In the present study, the colloidal particles were confined in a convex layer, and the growth front lay along the periphery of the substrate. Q. Yan *et al.* reported that colloidal crystallization can be achieved at the air–water interface *via* electrostatic interactions and lateral capillary forces. Based on the experimental results obtained in this study, we believe that the colloidal crystallization observed on a horizontal solid substrate, as reported here, is primarily driven by a convective self-assembly mechanism.

A colloidal suspension with a given concentration is deposited on an adequately treated substrate using a pipette, which allows for precise control of the drop volume. Then, the suspension is spread on the substrate. Due to the capillary forces, a small amount of the suspension may enter the pipette. When the syringe pipette is moved along the surface of the

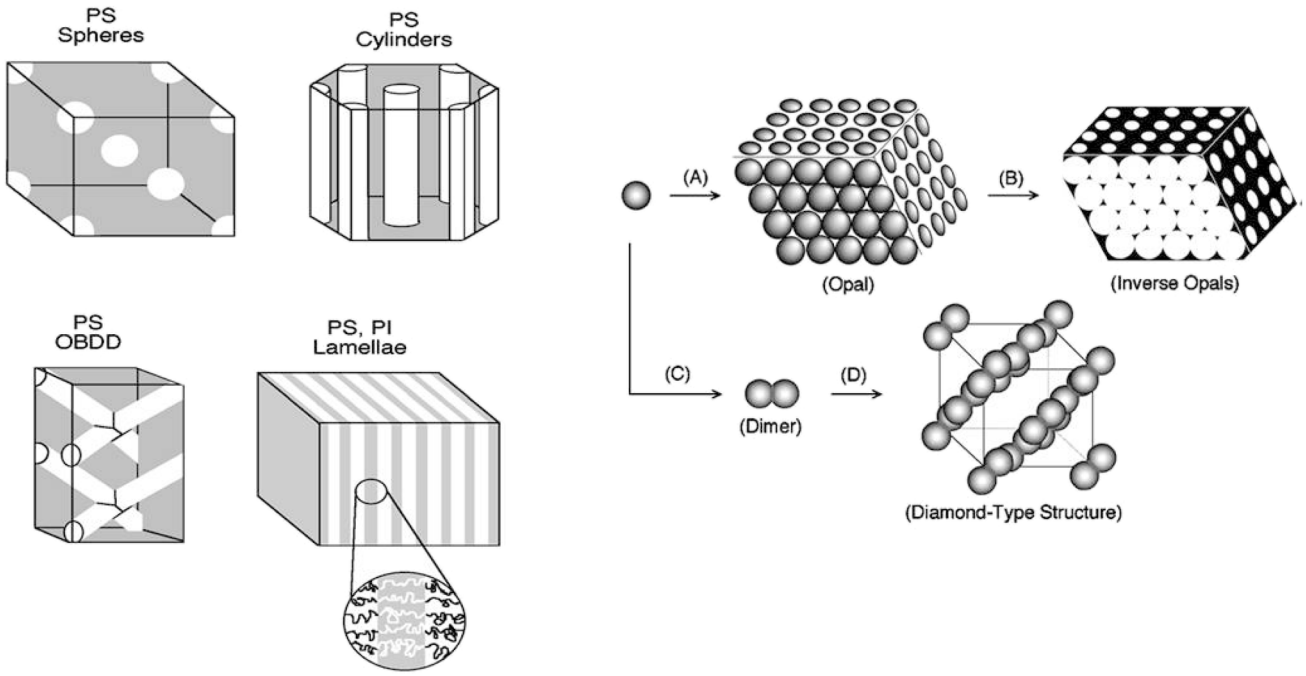

Fig. 6 Schematic illustrations of some typical mesoscale periodic structures that can be generated through the phase separation of organic block copolymers, such as polystyrene–polyisoprene (PS–PI). By varying the ratio between the chain lengths (or molecular weights) of these two units, one could obtain long-range ordered phases such as the 3D body-centered cubic lattice of PS spheres, the 2D hexagonal array of PS cylinders, the three-dimensionally ordered bi-continuous double diamond (OBDD) structure, and the 1D lamellae phase. Schematic illustrations of some 3D periodic structures that could be produced *via* the self-assembly of mono-dispersed spherical colloids: (A) the 3D opal (or cubic close-packed lattice) crystallized from spherical colloids; (B) the inverse (or inverted) opal made by templating against an opaline lattice; and (C and D) the diamond lattice generated *via* two-steps of self-assembly: formation of dimers from spherical colloids and crystallization of these dimers into an fcc lattice. Reproduced from ref. 91.

substrate, the colloidal suspension is guided to spread across the substrate and eventually fully cover the substrate surface, as illustrated in the second panel. The spread suspension is exposed to ambient conditions, and colloidal crystallization occurs. After 1–2 hours, a thin colloidal crystal film with a macroscopic void formed on its center is obtained.[16] When the colloidal suspension is deposited on a horizontal substrate, followed by careful spreading to cover the substrate surface fully, it has been observed that it begins to exhibit an iridescent color at the edge of the substrate after a few minutes, and the iridescent color gradually moved from the periphery toward the center of the substrate.[85]

2.2. Approaches of photonic crystals *via* the self-assembly method

Self-assembly represents an effective route to obtain well-defined 3D structures.[86–89] In this process, pre-designed building blocks (*e.g.*, molecules or mesoscale objects) could spontaneously organize themselves into a relatively stable (often long-range ordered) structure through non-covalent interactions. The critical idea in self-assembly is that the final structure is close to or at a thermodynamic equilibrium state.[90] Thus, such a process tends to reject defects and often leads to structures having a more excellent order than in non-self-assembling systems. The characteristics of the building blocks typically determine the final structure, as the information that defines the self-assembled structure is encoded in the building blocks through topologies, shapes, and surface functionalities. The inherently parallel nature of the self-assembly process makes this approach well-suited for a large-scale production process, in Fig. 6, where low cost and high throughput are the two key requirements.

2.3. Vertical deposition

Jiang *et al.*[92] first reported the vertical deposition method for creating 3D PhCs. This method involves placing a glass slide vertically into a beaker containing a suspension of particles. The colloidal suspension wets the glass, forming a meniscus where the substrate, air, and liquid meet. Capillary forces draw the spheres toward the substrate and attract them to each other, facilitating the formation of a close-packed monolayer. As solvent flows toward the meniscus and evaporates, particles deposit onto the slide, assembling into a colloidal crystal film (see Fig. 7). The film's thickness can be controlled by adjusting the particle concentration. Sedimentation is prevented by placing the solution in an oven at a fixed temperature, which is especially advantageous for polymer colloids in water due to their lower density difference compared to silica colloids.

2.4. Other methods

Various methods exist for self-assembling colloidal spheres into crystalline structures. For instance, electrophoretic deposition

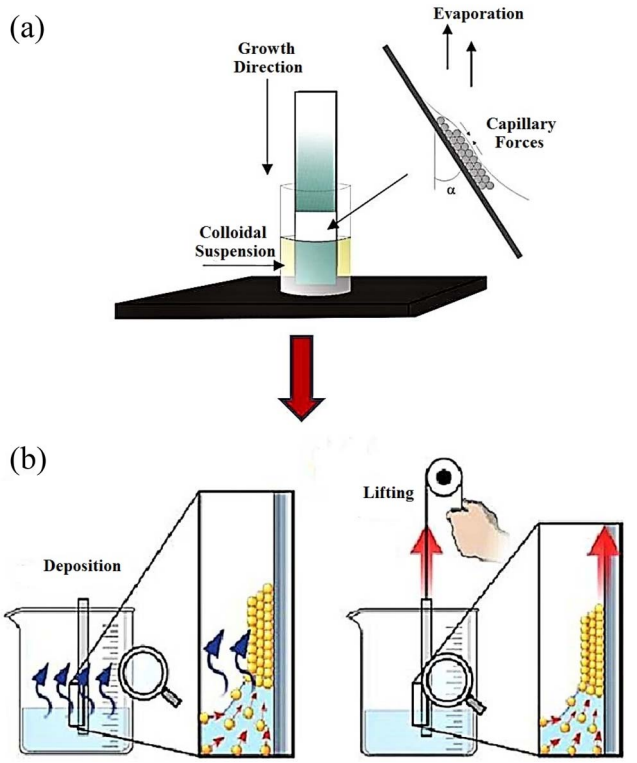

Fig. 7 Schematic illustration of vertical deposition (a) and lift-up deposition (b). Reproduced from ref. 93. Diagram of the vertical deposition method. Reproduced from ref. 94.

acts as a sedimentation technique that employs an external electric field to regulate the settling speed of surface-charged colloidal spheres. The doctor blade coating (DBC) method is likely derived from the physical confinement approach, where colloidal spheres are contained within a narrow gap between the blade and the substrate (Fig. 8(a)).[95–97] The immobilized blade exerts a unidirectional shear force on the confined colloidal suspension. The key force driving colloidal crystallization in this process remains the capillary force. Similarly, Park's group[98] developed a confined convective assembly method for quickly fabricating colloidal crystal films (Fig. 8(b)). In this technique, colloidal suspensions are confined between two vertical substrates. By adjusting the lift-up rate of one substrate, the meniscus height can be controlled. This allows both 2D and 3D PhCs to be deposited over large areas.

In summary, these methods offer a viable alternative due to their combined ease of fabrication, mass production, and low cost. Despite these tremendous advances, self-assembly methods often introduce random defects, such as missing particles, phase mixtures, uncontrolled orientation, boundary effects, and dislocations during the self-assembly process.

3. Self-assembly of colloidal PhCs & effects

Self-assembly techniques are considered the most practical approach for creating two-dimensional (2D) or three-dimensional (3D) photonic crystals (PhCs).[99–101] This process can be achieved through methods like gravity sedimentation, vertical deposition, horizontal deposition, among others. Among these, the vertical deposition method[102] is the most popular because it enables the production of large-area PhCs with controllable thickness and high quality, characterized by low defect density. The morphology and quality of PhCs can be managed by adjusting conditions such as temperature, air pressure, solvent type, and humidity during the self-assembly process. Manipulating colloidal particle self-assembly not only deepens our understanding of condensed matter physics but also broadens its applications to functional materials such as photonic waveguides, switches, optical filters, and sensors for chemical and biochemical detection.[103] In this study, we used self-assembled PhCs made from polymer colloids. Employing polymer colloids as building blocks enables cost-effective fabrication and precise control over properties such as chemical composition, particle size, and shape. Moreover, they can be easily removed *via* solvent dissolution or thermal treatment, making them suitable as templates for creating macroporous materials or inverse opals.[104]

High-quality crystals with low defect density are essential for the practical use of CPCs in photonic devices. However, fabricating a defect-free CPC on a large scale remains difficult. Capillary forces drive the evaporative self-assembly of CPCs at the meniscus of the colloidal suspension. Some control over CPC quality can be achieved by adjusting synthesis parameters,

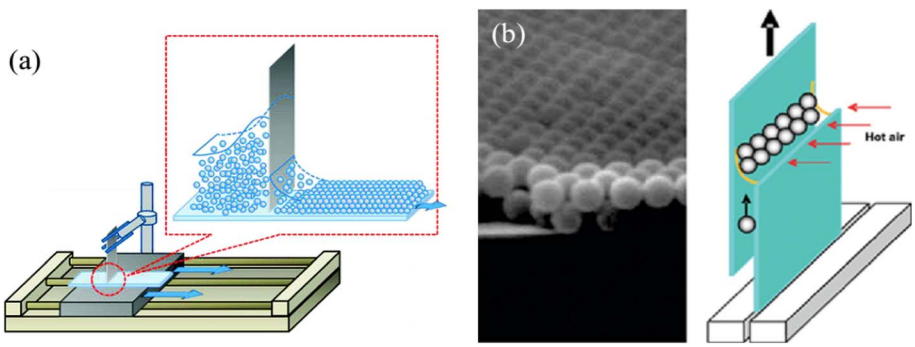

Fig. 8 Schematic illustration of the doctor blade coating method (a) (reproduced from ref. 98) and the confined convective assembly method (b) (reproduced from ref. 95).

such as temperature, air pressure, solvent type, humidity, and the speed of the contact line's movement. In 3-D photonic crystals formed by self-assembly, two critical defects are stacking faults and macroscopic cracks, which disrupt light propagation. Stacking faults, which occur between FCC and HCP structures, are likely due to their slight free energy difference. In contrast, macroscopic cracks result from crystal contraction during solvent evaporation.

3.1. Temperature

It is well known that maintaining the evaporation rate at an optimal value is crucial for producing high-quality photonic crystals. The high or low speed of solvent evaporation can induce stacking faults and macroscopic cracks in colloidal crystals. Temperature is considered a key factor in solvent evaporation, which also affects the self-assembly of colloidal particles.[105] It has been demonstrated that a high temperature will increase the kinetic energy of the colloidal particles, and only a poorly ordered array will be obtained. At the same time, a low temperature will cost too much time. So, the best compromise in terms of temperature should be found. Besides temperature, other growth parameters, such as air pressure, humidity, and solvent type, are also necessary for keeping the evaporation rate steady to obtain the optimal growing conditions for photonic crystal growth.

3.2. Air pressure

To determine the evaporation rate of the solvent according to the relation between pressure and the solvent's boiling point, the optimal heating temperature can also be significantly altered by changing the pressure. Zheng *et al.*[106] employed a controlled negative pressure during isothermal heating vertical deposition and found the optimal condition for making high-quality colloidal crystals by changing the pressure in a wide range. As a result of low pressure and low temperature, the materials of building blocks could be largely extended, especially for organic and biologically active materials.[105]

3.3. Solvent type

Solvent plays a crucial role in the self-assembly of photonic crystals. When these crystals are deposited onto solid substrates, contraction during solvent evaporation causes macroscopic cracks. This contraction results from the shrinkage of colloids and decreased separation between microspheres. Li and Marlow[107] examined how solvents impact 42 depositions of photonic crystals from colloidal suspensions of PS microspheres. Ethanol or water is commonly used as the solvent in most self-assembly processes, and mixtures of water and ethanol at various ratios have been employed to adjust properties like surface tension, viscosity, and volatility. Their findings indicated that the solvent significantly affects both the

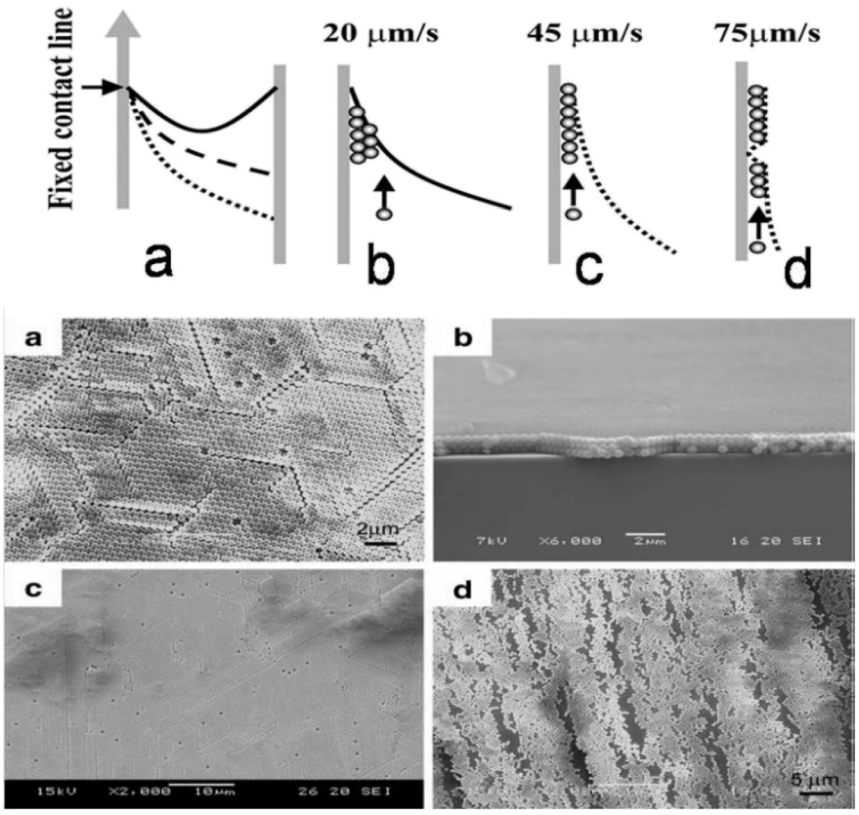

Fig. 9 Meniscus lift-up observed at different contact line speeds. The top panel shows schematic shapes of the meniscus at lift-up rates of 20 μm s^{-1}, 45 μm s^{-1}, and 75 μm s^{-1}. The bottom panel presents SEM images of the corresponding colloidal crystals: (a) 20 μm s^{-1}; (b) side view of a tri-layer at 20 μm s^{-1}; (c) 45 μm s^{-1}; (d) 75 μm s^{-1}. Reproduced from ref. 109.

surface morphology—such as crack distribution and film thickness—and the microstructure, including sphere ordering, of the photonic crystal films. The evidence that the solvent influences sphere self-assembly offers opportunities to control the film's morphology, enhance quality, and better understand the mechanisms behind different photonic crystal fabrication methods.

3.4. Humidity

High-quality photonic crystals can be obtained in a controlled high-humidity system, resulting from enhanced particle capillary forces. Chung *et al.*[108] discussed the effect of humidity on the quality of photonic crystals and the underlying mechanism governing the arrangement of colloids. They compared the morphology of photonic crystals obtained at evaporation temperatures of 70 °C, 60 °C, and 45 °C with constant high humidity (90%). High-quality colloidal crystals were fabricated at 45 °C and 90% humidity in 24 h, while only poorly ordered structures were obtained at the other two temperatures. However, when the temperature is 45 °C and the humidity is 40% or 60%, the quality of photonic crystals remains poor, indicating that humidity is a significant factor in controlling the quality of photonic crystals. It was proved that the effect of capillary force increased with increasing humidity levels. In contrast, the capillary force could fine-tune the relative position of the neighboring colloids and efficiently decrease the number of defects, resulting in the formation of perfect photonic crystals.

3.5. Moving speed of the contact line

During evaporative assembly, the highest solvent evaporation rate appears at the edge of the colloidal suspension. In most cases, the self-assembly of colloids into ordered structures starts at the contact line between the substrate, the suspension, and the air. As the contact line moves with the lowering of the liquid surface by solvent evaporation, colloidal crystals form on the substrate. The movement of the contact line can be controlled by lifting the substrate out of the suspension at a constant speed. Kim *et al.*[109] and Ko and Shin investigated the relationship between the morphology of colloidal crystals and the lift-up speed. They found that the lift-up speed could control the colloidal structure at a fixed concentration (Fig. 9). An appropriate lift-up speed was found to obtain mono-layered colloidal crystals over a large area. At a lower lift-up speed, multi-layered colloidal crystals were obtained, because more colloidal particles moved to the contact line in the same period. A structure 43 with low coverage was obtained at a higher lift-up speed because the colloidal particles have insufficient time to move up to the contact line. In the case of multilayered colloidal crystals, the film thickness can be controlled by adjusting the lift-up speed.

4. Applications of colloidal crystals

This section discusses recent examples of polymer colloidal crystals used for various potential applications. These investigations are based on their optical properties, chemical composition, and nanostructures.

4.1. Laser application

In colloidal crystals, certain wavelengths of light cannot propagate in specific directions, and this makes them useful in optical devices.[110] Researchers developed a new application of colloidal crystals as flexible polymer laser devices with low-threshold optical excitation. They placed a light-emitting polymer layer between two colloidal crystal films, creating a planar

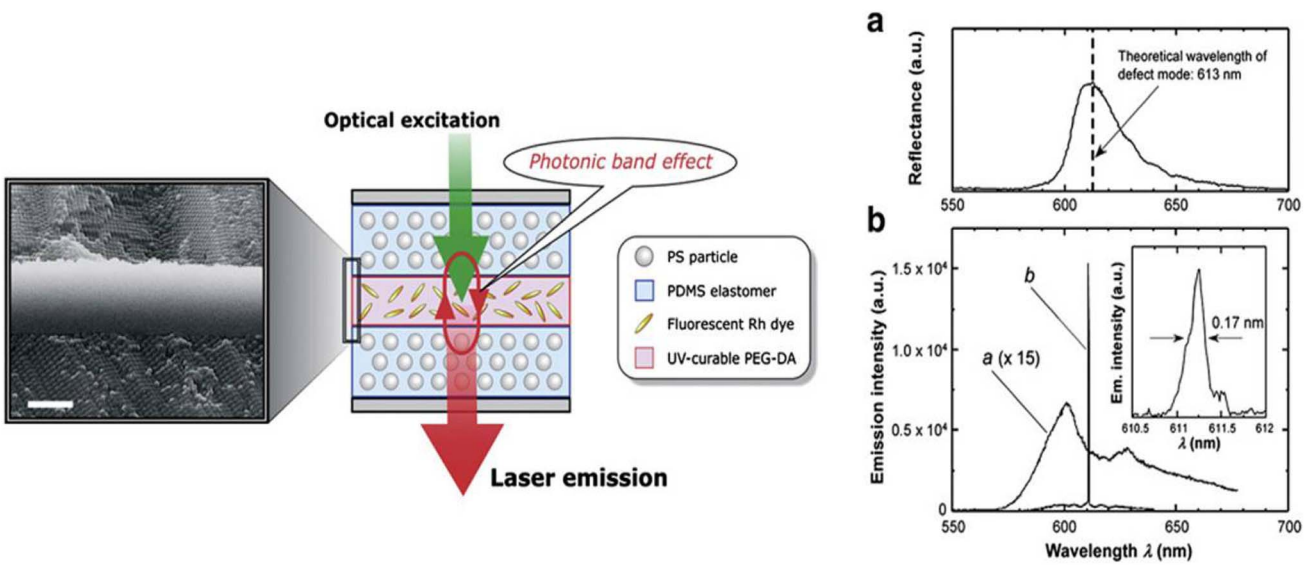

Fig. 10 Schematic illustration of the colloidal crystal laser device and the reflection spectrum (a) and emission spectra (b) from the device. Emission spectra were obtained from optical excitation with second-harmonic light at 532 nm from a Nd:YAG laser beam with an energy of 70 nJ per pulse (a) and 210 nJ per pulse (b) (reproduced from ref. 110).

defect (see Fig. 10). By aligning the stop-band of the crystal films with the dye's maximum fluorescence wavelength in the defect layer, efficient laser feedback occurs thanks to the photonic bandgap effect. Successful photon confinement from the light-emitting layer within the laser cavity enabled low-threshold lasing.[111] These advances represent a significant step toward developing lightweight, affordable, and flexible lasers for photonics and optoelectronics.[112] Additionally, colloidal crystals show promise as effective, selective reflection mirrors in optoelectronic and lighting devices.[113]

4.2. DSSC application

The use of self-assembled colloidal crystals in dye-sensitized solar cells (DSSCs) has also garnered significant interest in recent years.[114–120] DSSCs are an exciting alternative to conventional solid-state semiconductor photovoltaic devices, primarily due to their low production cost.[121] Miguez and co-workers conducted theoretical investigations into the effect of a photonic crystal on the optical absorption of DSSCs. They concluded that significant light absorption amplification occurred over a wide spectral range in structures that combined the presence of a photonic crystal and a layer of nanocrystalline absorbing material, and that the absorption enhancement occurs in resonant modes localized within the absorbing nanocrystalline coating.[122] In addition, it was predicted that the stacking of crystals with different lattice constants could lead to enhanced light harvesting across the entire dye absorption range.[123] Several strategies have since been developed to combine photonic crystals and DSSCs by self-assembly techniques. Zhang *et al.* demonstrated photonic crystal concentrators for DSSCs made by self-assembling latex spheres on concave watch glasses. They concluded that the wavelength-selective photonic crystal concentrator can improve the maximum power of the DSSC by more than five times while retaining a stable, high performance (Fig. 11).[124]

4.3. Light emitting diode application

An *et al.* discussed using cone-shaped deep-pillar nanostructures to enhance light extraction in honeycomb-type vertical GaN light-emitting diodes (VLEDs). They created these cone-shaped pillars by spin-coating polystyrene nanospheres onto n-GaN substrates, then etching the surface with oxygen plasma. Their findings showed that this structure increased VLED output power by up to 214% at 350 mA compared to a reference device, likely due to multiple light scattering from the cones' sidewalls (Fig. 12).[125]

Li *et al.* explained how nanosphere lithography was used to create a close-packed array of nanopillars embedded within an InGaN/GaN LED structure. This periodic, ordered nanopillar arrangement enhances light extraction and reduces the piezoelectric field by relaxing strain in the InGaN/GaN quantum wells. They noted that LEDs with embedded photonic crystals produce up to 20% more light compared to the reference LED (see Fig. 12).[126]

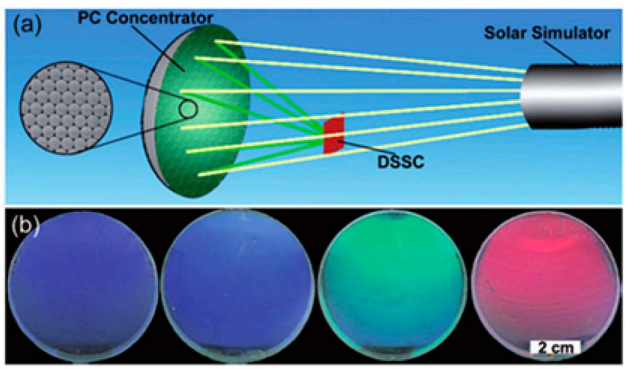

Fig. 11 (a) Schematic illustration of the photovoltaic system with a photonic crystal concentrator. The inset is an SEM image of the photonic crystal concentrator. (b) Photographs of the PC concentrators with different colors.[124]

4.4. Effect of the 3DOM structure on photogenerated carriers and efficient photocatalytic hydrogen production performance of 3DOM CdS

Time-resolved photoluminescence (TRPL) decay spectra and electrochemical impedance spectra (EIS) were measured to investigate the effect of the 3D ordered macroporous (3DOM) structure on the trapping, recombination, and migration of photogenerated carriers. The blue shift in Fig. 13 corresponds to the PL emission peak, further demonstrating the broadening of the band gap in the 3DOM CdS. The CdS nanoparticles demonstrate a more substantial PL emission peak than the 3DOM CdS, indicating that the recombination rate of photo-excited carriers is considerably reduced by constructing the 3DOM structure. The fact that the TRPL decay spectrum of the 3DOM CdS exhibits a longer carrier lifetime than the CdS nanoparticles further confirms that the photogenerated electrons and holes are effectively separated.[127,128] As shown in Fig. 13, the Nyquist circle diameter of 3DOM CdS is much smaller than that of the CdS nanoparticles, indicating that the transport resistance of 3DOM CdS is significantly reduced, and the electron mobility is enhanced. The reasons for the change of the photogenerated carrier states are explained in Fig. 13. The high recombination rate of carriers should be ascribed to the aggregation of the CdS nanoparticles, leading to the tremendous increase in grain boundaries and easy driving of the recombination of photogenerated electrons and holes.[129] On the contrary, the 3DOM CdS with an open, interconnected spherical void structure effectively reduces the number of grain boundaries and provides a prodigious surface area for charge separation.[130] In addition, the rapid electron mobility is attributed to the periodic structure of 3DOM CdS, which endows it with a uniform and symmetrical thin wall, resulting in a short diffusion length of photoinduced carriers.[131] More importantly, the 3DOM CdS has a hierarchical porosity compared to single-sized porous materials. Based on Murray's law, the hierarchical networks of pores can maximize material transport and achieve a high reaction rate.[132–134] Therefore, the interconnected porosity of different sizes will improve mass transport, increase the selectivity on the level of pores, and reduce the migration resistance of carriers.

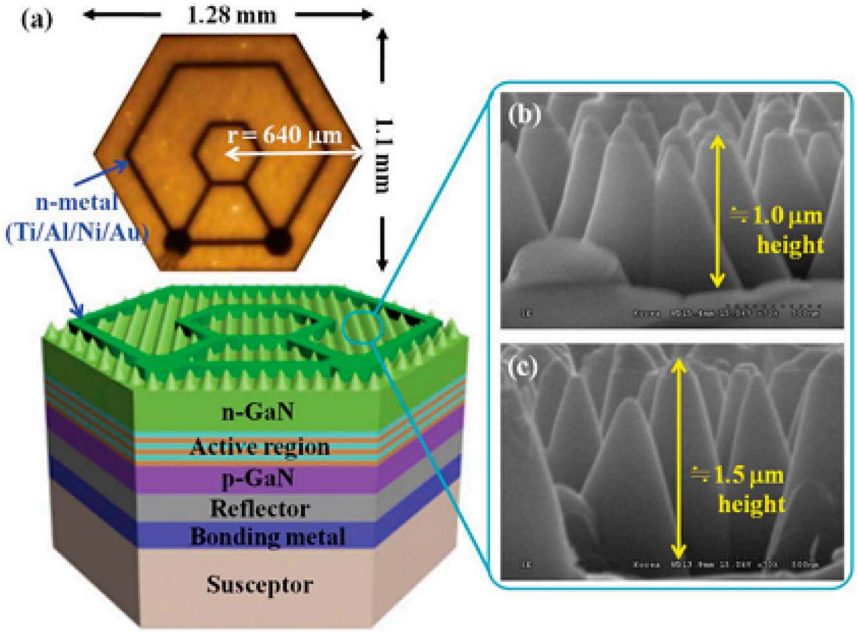

Fig. 12 Honeycomb-type VLED with a textured cone-shaped deep-pillar surface.[125]

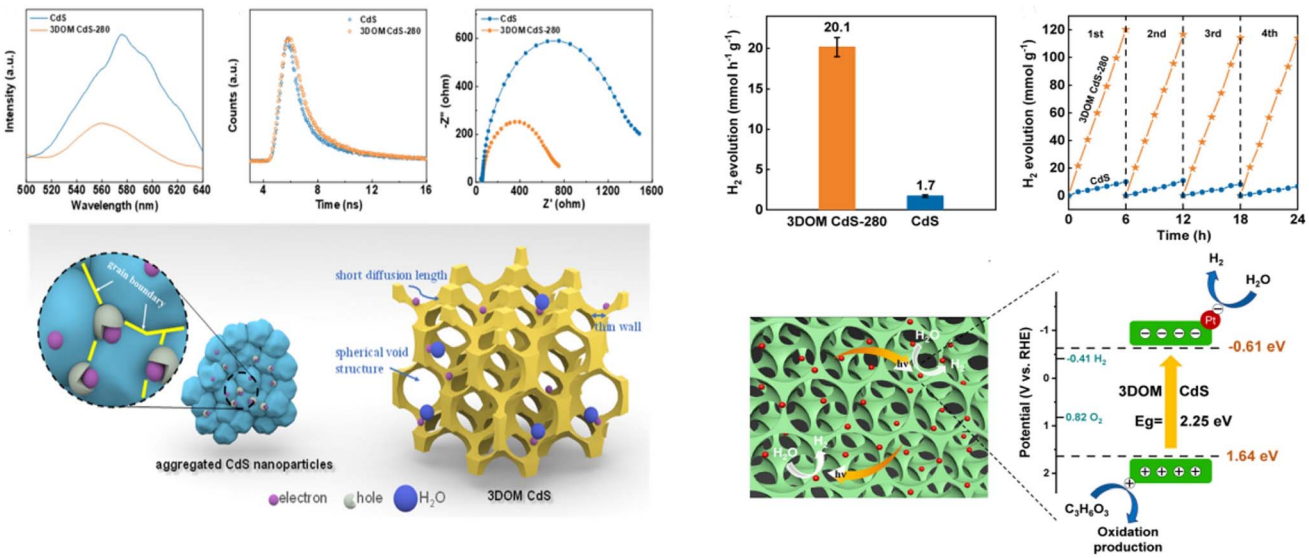

Fig. 13 Temperature-dependent emission spectra, TRPL decay spectra, EIS-Nyquist diagrams, and schematic representation of the photogenerated carrier states of CdS nanoparticles and 3DOM-CdS. Production rates of photocatalytic H_2 and recyclability tests of 3DOM CdS and CdS nanoparticles with 0.3 wt% Pt loading, and schematic representation of 3DOM CdS for photocatalytic H_2 production.

The photocatalytic H_2 production rates of 3DOM CdS and the CdS nanoparticles loaded with 0.3 wt% Pt were evaluated using lactic acid as the sacrificial reagent, as shown in Fig. 13. The hydrogen evolution rate of 3DOM CdS is substantially promoted to 20.1 mmol h^{-1} g^{-1} from only 1.7 mmol h^{-1} g^{-1} of the CdS nanoparticles. The 3DOM structure has a significant influence on the photocatalytic activity of CdS. To investigate the stability of 3DOM CdS, cyclic hydrogen evolution is tested, as shown in Fig. 13. The photocatalytic activity of 3DOM CdS has no apparent attenuation after four cycles of catalytic reaction, but the CdS nanoparticles began to show a decrease after the first two cycles. This phenomenon suggests that the 3DOM structure is also favorable for improving stability. This is primarily due to the excellent mass transfer performance of 3DOM CdS and its ability to exchange material with lactic acid efficiently. Hence, more holes can be consumed to reduce the occurrence of photocorrosion. In addition, 3DOM CdS was tested under visible light ($\lambda \geq 420$ nm), and we can find that 3DOM CdS possesses an excellent and stable visible light photocatalytic hydrogen production performance, which is mainly caused by the

retention of the promising visible light response of CdS in 3DOM CdS.

4.5. Printing on membrane surfaces

Electrospinning. Electrospinning utilizes electrical forces to draw charged polymer solutions or melts into fibers, resulting in diameters of just a few hundred nanometers. It shares characteristics with electrospraying and traditional dry spinning of fibers. The process does not need coagulation chemistry or high heat to form solid filaments, making it ideal for creating fibers with large and complex molecules. Additionally, electrospinning from molten precursors is employed, which prevents any solvent from entering the final product.

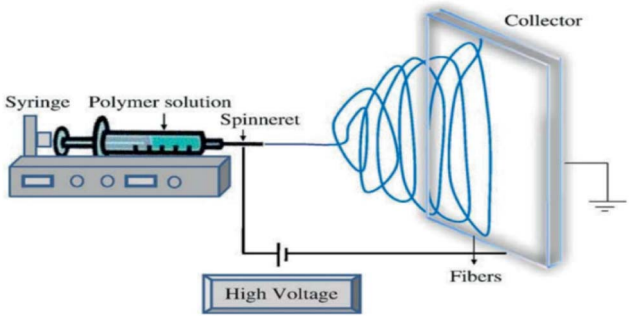

Experimental set-up of electrospinning. The 3D printing technology for fabricating the whole membrane is still under development. However, more realistic studies based on current technology can be seen in research regarding the inkjet printing or 3D printing of solvents or gels on the surface of membranes.

Introducing inkjet printing applications brought new approaches to synthesizing a selective layer of water treatment membranes. Gao *et al.* further developed the technology by synthesizing polymeric nanomaterials, including polymeric nanotubes, nanowires, and thin films.[135] To achieve the final form of the PCTE membranes, polymeric, carbon, metallic, and semiconducting materials were deposited inside the membrane's pores to obtain nanotubes or nanowires. As a result, reasonable performance in terms of salt rejection and water flux was obtained for the inkjet-printed nanofiltration membranes.[136] Later, Gao *et al.* used the same approach, preparing poly(vinyl alcohol)-based composite inks containing poly(diallyldimethylammonium chloride) or poly(sodium 4-styrene sulfonate) to apply patterns with domains of ordered positive and negative charges to the surface of polycarbonate track-etched membranes. Having the same amount of positive and negative charge domains resulted in a neutral charge, which increased the permeation of the mosaic membrane. Unlike other researchers, Lee and Heo *et al.* utilized silver nanoparticles to print on electro-spun polyurethane fibrous membranes using inkjet printing (Fig. 14). Silver nanoparticle-printed membranes showed bacterial resistance during water purification.[137]

Recently, Bernstein *et al.* utilized inkjet printing and graft polymerization surface modification of polymeric membranes (Fig. 15). In their research, polyether sulfone UF membrane surfaces were coated with [2-(methacryloyloxy)ethyl]dimethyl-(3-sulfopropyl)ammonium hydroxide dissolved in base ink and then irradiated with UV light. The modified membranes yielded low protein fouling properties and less biofilm growth (Fig. 15).[138] Since carbon-based materials, especially graphene oxide (GO), were attracting much attention because of their highly enhanced performance for water treatment membranes,[139–147] Fathizadeh *et al.* used inkjet printing to obtain ultrathin GO membranes. GO "ink" was prepared by dispersing 400 mg of single-layer graphene oxide (SLGO) in 100 mL DI water. After different concentrations of GO inks were prepared by dilution, a commercial printer was used to coat the M-PAN support with GO ink followed by drying procedures (Fig. 15).

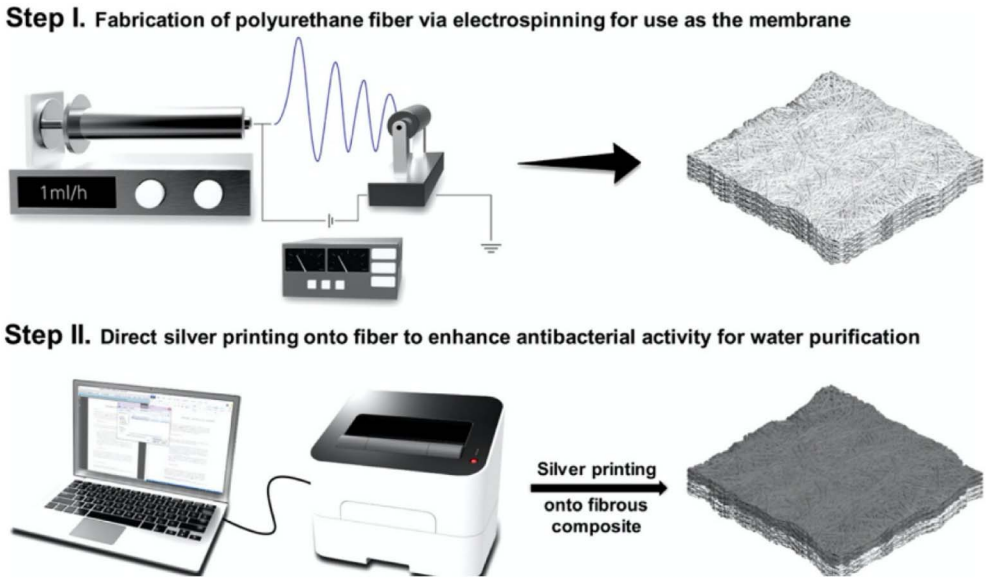

Fig. 14 teps of the electro-spun membrane printing process. The image is reproduced from a previous study[137] with permission from Elsevier.

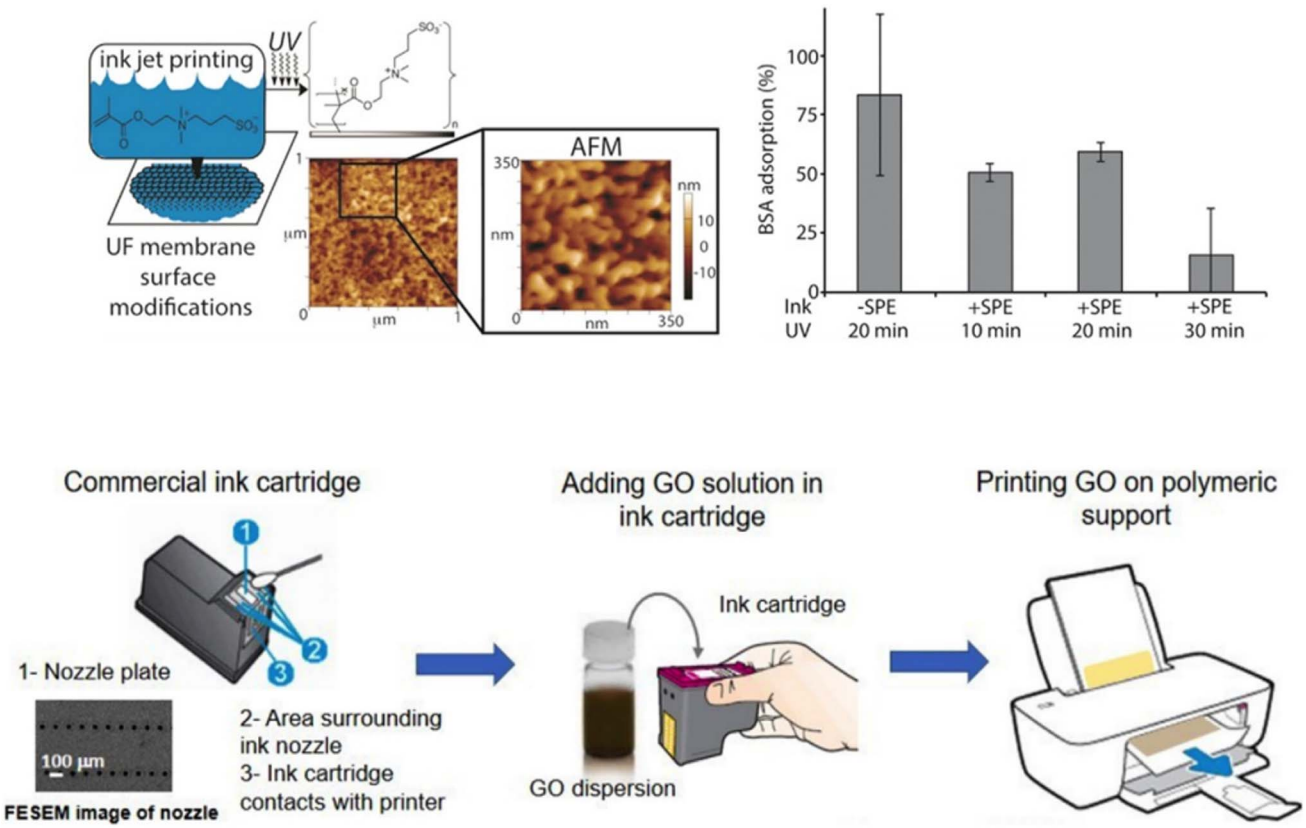

Fig. 15 This figure shows an atomic force microscopy (AFM) image of polymer membranes modified by inkjet printing and graft polymerization, reproduced from a previous study[122] with permission from Elsevier. Also included is a schematic diagram of the process for printing ultrathin GO membranes, taken from an earlier study[148] with permission from the Royal Society of Chemistry.

4.6. Deep learning for topological photonics

Topological photonics has garnered significant interest due to its unique properties, such as unidirectional electromagnetic wave propagation and robust photon control. These features are promising for advancing next-generation nano-photonic devices. However, modeling and designing these complex systems present considerable challenges. Recently, deep learning (DL), a subset of machine learning that utilizes neural network (NN) algorithms, has emerged as an effective tool in nanophotonics for capturing intricate nonlinear relationships between design parameters and optical outcomes. Particularly in nano-photonics, DL applications powered by NN models have achieved remarkable success in understanding the overall material properties of topological systems.

Inspired by human learning, DL and other machine learning algorithms use data and experience to discover the implicit rules governing a system. The training data are processed and analyzed to develop an approximate, data-driven model. For tasks like predicting specific values, decision-making, or generating new samples, machine learning aims to create models that perform these functions without explicit programming. Standard functions include regression, classification, clustering, and dimensionality reduction—all supported by various algorithms.

The architecture resembles a brain's neural network, where each neuron performs an affine transformation of inputs using weights and biases, and then passes the result through a nonlinear activation function (see Fig. 16(a)). When neurons are organized into multiple layers (see Fig. 16(b)) with trained weights, the entire network functions as an approximate model capable of performing the desired task. The term 'deep' in deep learning refers to the use of multi-layered neural networks; currently, these can have up to hundreds of layers.

To train an NN, a loss function must be defined first. A loss function is a function that quantifies the difference between the desired output (ground truth) and the output produced by the NN model. Depending on the type of task desired, an appropriate loss function should be chosen and adapted. Commonly used loss functions include the mean squared error for regression problems and the cross-entropy loss for classification problems. The weights of the NN are then adjusted to minimize this distance by using the gradient descent rule with an algorithm called backpropagation[149,150] (Fig. 16(c)). In every iteration of the forward pass of the input data batch, it computes the gradient of the loss function concerning each weight and bias using the chain rule, starting from the end of the NN and working backward. The weights are then updated through iterations of gradient descent with a user-defined

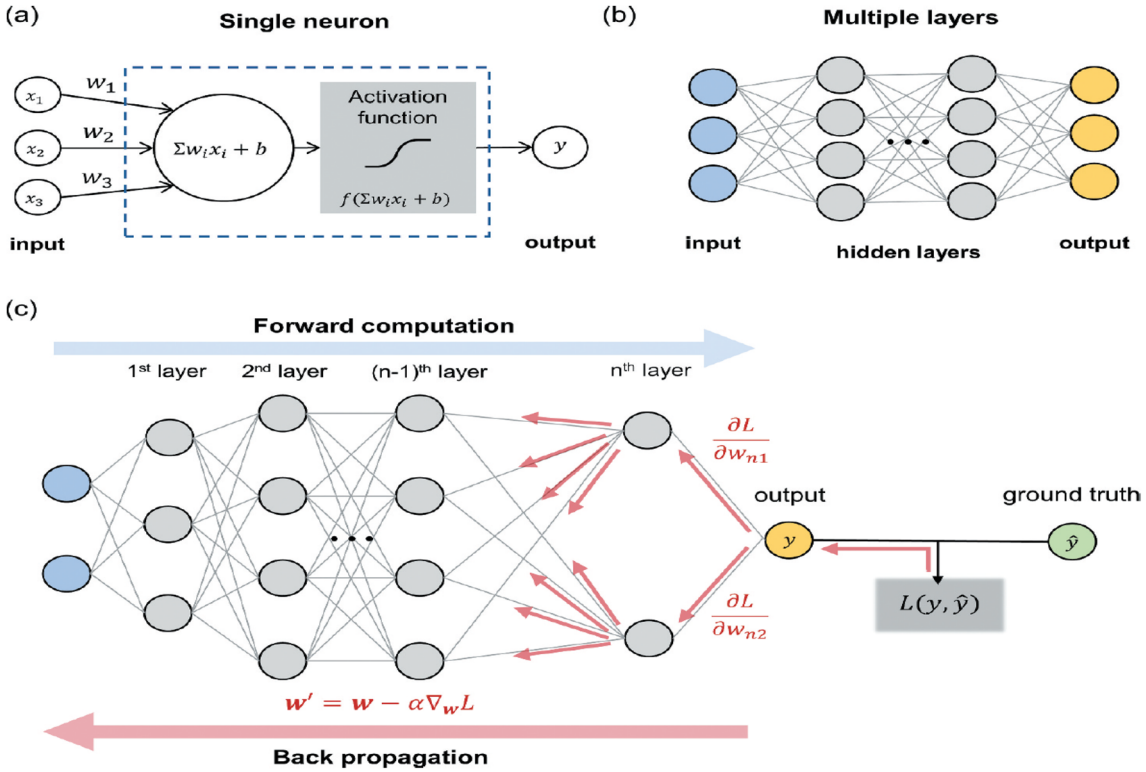

Fig. 16 Schematic illustration of a neural network (NN). (a) A single neuron calculates a weighted sum of inputs and adds a bias term, followed by a nonlinear activation function. The output value is passed as an input to the next layer. (b) A fully connected, multiple-layered NN. When an NN is adequately trained, it learns the generalized, nonlinear relationship between the input (blue nodes) and the output (yellow nodes). (c) Schematic of NN training. The gradient of the loss function L with respect to each weight and bias value is calculated using the backpropagation algorithm. The input data batch is passed forward, and every partial derivative of the learnable parameters is calculated from back to front. The weights are updated by the gradient descent rule with a defined learning rate α iteratively. The weight w_{ij} represents the j^{th} from the i^{th} layer to the next.

hyperparameter called the learning rate that determines the step size of each iteration.[151–153]

5. Conclusions

This review discusses various aspects of self-assembly, including different types of self-assembly, such as molecular, colloidal, and macroscopic self-assembly, as well as their driving forces, including thermodynamic equilibria, kinetic control, and external field-directed organization. The examples presented are diverse in their scales, structures, and properties, ranging from atomic-level DNA origami to micrometer-scale colloidal crystals and even larger metamaterials. Due to the broad scope of this challenging science, which encompasses chemistry, physics, materials science, and engineering, it isn't easy to draw a definitive conclusion within a single field. This review examines the fundamental concepts and recent advances in innovative, tailored self-assembly processes for nanophotonic crystals, including block copolymer templating, DNA-guided assembly, and evaporative colloidal crystallization, as well as their latest applications in artificial intelligence, such as optical neural networks and neuromorphic computing. We have also explored the possibilities of using self-assembled photonic crystals as templates for fabricating inverse opals with tunable bandgaps, as well as nanosphere lithography for plasmonic metasurfaces, highlighting their potential applications in sensing, light harvesting, and quantum optics. This review provides a clear introduction to AI-based self-assembled photonic crystals for newcomers to the field, covering essential principles such as Bragg diffraction and Mie resonances, while also offering new insights and ideas for experienced researchers, including machine learning-optimized self-assembly protocols and autonomous material discovery platforms. While there is still much more to discover about the associated physics and chemistry of these materials, including defect dynamics, non-equilibrium phenomena, and interfacial interactions, it is only a matter of time before the next leap is made toward better understanding, improved fabrication technologies, and innovative new applications for the future, such as adaptive camouflage, ultra-efficient lasers, and bio-hybrid optical systems. Overall, by addressing challenges in scalability, reproducibility, and integration, while exploiting breakthroughs in computational design, *in situ* characterization, and multi-material self-assembly, the science of self-assembly is poised to revolutionize photonics, nanotechnology, and intelligent material systems in the coming decades.

In summary, while machine learning is transforming self-assembly research, overcoming data limitations, improving multi-scale modeling, and enhancing experimental integration

will be critical for fully realizing its potential in nanophotonics and beyond.

Conflicts of interest

The authors declare no conflict of interest.

Data availability

No primary research results, software or code have been included and no new data were generated or analysed as part of this review.

References

1 W. Ma, *et al.*, Deep learning for the design of photonic structures, *Nat. Photonics*, 2021, **15**(2), 77–90.
2 Y. Liu, *et al.*, Structural color three-dimensional printing by shrinking photonic crystals, *Nat. Commun.*, 2019, **10**(1), 4340.
3 W.-Z. Ma, *et al.*, VO2-based thermally tunable emitter and preliminary design of switching for mid-infrared atmospheric windows, *Results Phys.*, 2021, **31**, 105055.
4 R. Karyappa, *et al.*, Digital fabrication of colors with colloidal crystals and colloidal glasses, *Next Nanotechnol.*, 2024, **6**, 100062.
5 V. R. Balaji, Machine learning enabled 2D photonic crystal biosensor for early cancer detection, *Measurement*, 2024, **224**, 113858.
6 W. Sen, *et al.*, Effects of human–machine interaction on employee's learning: a contingent perspective, *Front. Psychol.*, 2022, **13**, 876933.
7 E. Yablonovitch, *Phys. Rev. Lett.*, 1987, **58**, 2059.
8 S. John, *Phys. Rev. Lett.*, 1987, **58**, 2486.
9 P. Jiao and A. H. Alavi, Artificial intelligence-enabled smart mechanical metamaterials: advent and future trends, *Int. Mater. Rev.*, 2020, **66**, 365–393.
10 O. Sigmund and J. S. Jensen, Systematic design of phononic band-gap materials and structures by topology optimization, *Philos. Trans. R. Soc., A*, 2003, **361**, 1001–1019.
11 B. Ahn, H. Lee, J. S. Lee and Y. Y. Kim, Topology optimization of metasurfaces for anomalous reflection of longitudinal elastic waves, *Comput. Methods Appl. Mech. Eng.*, 2019, **357**, 112582.
12 J. Rong and W. Ye, Multifunctional elastic metasurface design with topology optimization, *Acta Mater.*, 2020, **185**, 382–399.
13 Y. Elesin, B. S. Lazarov, J. S. Jensen and O. Sigmund, Time domain topology optimization of 3D nanophotonic devices, *Photonics Nanostruct.*, 2014, **12**, 23–33.
14 S. Russell and P. Norvig, *Artificial Intelligence: A Modern Approach*, Prentice-Hall, Englewood Cliffs, US, 2009.
15 M. I. Jordan and T. M. Mitchell, Machine learning: trends, perspectives, and prospects, *Science*, 2015, **349**, 255–260.
16 W. S. McCulloch and W. Pitts, A logical calculus of the ideas immanent in nervous activity, *Bull. Math. Biophys.*, 1943, **5**, 115–133.
17 D. O. Hebb, *The Organization of Behavior*, Taylor & Francis, London, UK, 2002.
18 F. Rosenblatt, The perceptron: a probabilistic model for information storage and organization in the brain, *Psychol. Rev.*, 1958, **65**, 386–408.
19 D. Rumelhart, G. Hinton and R. Williams, Learning representations by back propagating errors, *Nature*, 1986, **323**, 533–536.
20 M. Rosenblatt, *et al.*, *Nat. Commun.*, 2024, **15**, 1829.
21 Y. LeCun, Y. Bengio and G. Hinton, Deep learning, *Nature*, 2015, **521**, 436–444.
22 G. E. Hinton, S. Osindero and Y.-W. Teh, A fast learning algorithm for deep belief nets, *Neural Comput.*, 2006, **18**, 1527–1554.
23 M. Abadi, A. Agarwal, P. Barham, *et al.*, TensorFlow: Large-Scale Machine Learning on Heterogeneous Distributed Systems, *arXiv*, 2016, preprint, arXiv:1603.04467, DOI: 10.48550/arXiv.1603.04467.
24 A. Paszke, S. Gross, F. Massa, *et al.*, PyTorch: an imperative style, high-performance deep learning library, in *33rd Conference on Neural Information Processing Systems (NeurIPS 2019)*, Vancouver, Canada, 2019.
25 F. Chollet, *Deep Learning with Python*, Manning Publications, Greenwich, US, 2015.
26 A. Krizhevsky, I. Sutskever and G. E. Hinton, ImageNet classification with deep convolutional neural networks, *Commun. ACM*, 2017, **60**, 84–90.
27 K. Cho, B. Van Merriënboer, C. Gulcehre, *et al.*, Learning phrase representations using RNN encoder–decoder for statistical machine translation, in *Proceedings of the 2014 Conference on Empirical Methods in Natural Language Processing (EMNLP)*, Association for Computational Linguistics, Doha, Qatar, 2014, pp. 1724–1734.
28 A. B. Nassif, I. Shahin, I. Attili, M. Azzeh and K. Shaalan, Speech recognition using deep neural networks: a systematic review, *IEEE Access*, 2019, **7**, 19143–19165.
29 D. Silver, A. Huang, C. J. Maddison, *et al.*, Mastering the game of Go with deep neural networks and tree search, *Nature*, 2016, **529**, 484–489.
30 K. Noda, H. Arie, Y. Suga and T. Ogata, Multimodal integration learning of robot behavior using deep neural networks, *Robot. Autonom. Syst.*, 2014, **62**, 721–736.
31 K. R. Maskaly, W. C. Conter, R. D. Averitt and J. L. Maxwell, *Opt. Express*, 2005, **13**, 8380–8389.
32 K. Inoue, M. Wada, K. Sakoda, A. Yamanaka, M. Hayashi and J. W. Haus, *Jpn. J. Appl. Phys.*, 1994, **33**, L1463–L1465.
33 T. Zhang, J. Brown, R. J. Oakley and C. F. J. Faul, Towards functional nanostructures: ionic self-assembly of polyoxometalates and surfactants, *Curr. Opin. Colloid Interface Sci.*, 2009, **14**(2), 62–70.
34 C. Lopez, Materials Aspects of Photonic Crystals, *Adv. Mater.*, 2003, **15**(20), 1679–1704.
35 H. R. Vutukuri, J. Stiefelhagen, T. Vissers, A. Imhof and A. van Blaaderen, Bonding Assembled Colloids without Loss of Colloidal Stability, *Adv. Mater.*, 2012, **24**, 412–416.
36 R. Sapienza, M. Leonetti, L. S. Froufe-Pérez, J. F. Galisteo-López and C. López, Optical amplification enhancement

in photonic crystals, *Phys. Rev. A:At., Mol., Opt. Phys.*, 2011, **83**(2), 1–5.
37 M. A. C. Stuart, W. T. S. Huck, J. Genzer, M. Müller, C. Ober, M. Stamm, G. B. Sukhorukov, I. Szleifer, V. V. Tsukruk, M. Urban, F. Winnik, S. Zauscher, I. Luzinov and S. Minko, Emerging applications of stimuli–responsive polymer materials, *Nat. Mater.*, 2010, **9**(2), 101–113.
38 U. Biswas, *et al.*, Fabrication techniques and applications of two-dimensional photonic crystal: history and the present status, *Opt. Eng.*, 2022, **62**(1), 010901, DOI: 10.1117/1.OE.62.1.010901.
39 J. R. Wendt, G. A. Vawter, P. L. Gourley, T. M. Brennan and B. E. Hammons, *J. Vac. Sci. Technol., B:Microelectron. Nanometer Struct.–Process., Meas., Phenom.*, 1993, **11**, 2637–2640.
40 S. Noda, A. Chutnan and M. Imada, *Nature*, 2000, **407**, 608–610.
41 N. Yamamoto, S. Noda and A. Chutinan, *Jpn. J. Appl. Phys.*, 1998, **37**, L1052–L1054.
42 J. G. Fleming and S. Y. Lin, *Opt. Lett.*, 1999, **24**, 49–51.
43 S. Noda, N. Yamamoto and A. Sasakti, *Jpn. J. Appl. Phys.*, 1996, **35**, L909–L912.
44 S. Y. Lin, J. G. Fleming, D. L. Hetherington, B. K. smith, R. Biswas, K. M. Ho, M. M. Sigalas, W. Zubrzycki, S. R. kurtz and J. Bur, *Nature*, 1998, **394**, 251–256.
45 S. Noda, K. Tomoda, N. Yamamoto and A. Chutinan, *Science*, 2000, **289**, 604–606.
46 O. D. Velev, T. A. Jede, R. F. lobo and A. M. Lenhoff, *Nature*, 1997, **389**, 60–64.
47 A. A. Zakhidov, R. H. Baughman, Z. Iqbal, C. Cui, I. Khayrullin, S. O. Dantas, J. Marti and V. G. Ralchenko, *Science*, 1998, **282**, 897–901.
48 A. Blanco, E. Chomski, S. Grabtchak, M. Ibisate, S. John, S. W. Leonard, C. Lopez, F. Mesegner, H. Miguez, J. P. Mondia, G. A. Ozin, O. Toader and H. M. Van Driel, *Nature*, 2000, **405**, 437–400.
49 V. N. Astratov, Y. A. Vlasov, O. Z. Karimov, A. A. Kaplyanskii, Y. G. Musikgim, N. A. Bert, V. N. Bogomolov and A. V. Prokofiev, *Phys. Lett. A*, 1996, **222**, 349–353.
50 R. Mayoral, J. Requena, J. S. Moya, C. Lopez, A. Cintas, H. Miguez, F. Meseguer, L. Vazquez, M. Holgado and A. Blanco, *Adv. Mater.*, 1997, **9**, 257–260.
51 P. Jiang, J. Bertone, K. Hwang and V. Colvin, *Chem. Mater.*, 1999, **11**, 2132–2140.
52 R. V. Nair and R. Vijaya, *Nano Trends*, 2006, **1**, 12–16.
53 R. V. Nair and R. Vijaya, *J. Phys. D:Appl. Phys.*, 2007, **40**, 990–997.
54 Q. Yan, Z. Zhou and X. S. Zhao, *Langmuir*, 2005, **21**, 3158–3164.
55 R. V. Nair and R. Vijaya, *Appl. Phys. A*, 2008, **90**, 559–563.
56 S. Noda, A. Chutinan and M. Imada, *Nature*, 2000, **407**, 608–610.
57 O. Painter, R. K. Lee, A. Scherer, A. Yariv, J. D. O. Brien, P. D. Dapkus and I. Kim, *Science*, 1999, **284**(5421), 1819–1821.
58 H. G. Park, S. H. Kim, S. H. Kwon, Y. G. Ju, J. K. yang, J. H. Baek, S.-B. Kim and Y. H. Lee, *Science*, 2004, **305**, 1444–1447.
59 L. Hu, *et al.*, Self-assembly Fabrication and Applications of Photonic Crystal Structure Color Materials, *Acta Chim. Sinica*, 2023, **81**(7), 809–819.
60 K. Sakoda, *Optical Properties of Photonic Crystals*, Springer-Verlag, Berlin, 2001.
61 J. Bravo-Abad, A. Rodriguez, P. Bermel, S. G. Johnson, J. D. Joannopoulos and M. Sojacic, *Opt. Express*, 2007, **15**, 16161–16176.
62 P. P. Markowicz, H. Triyaki, H. Pudavar, P. N. Prasad, N. N. Lepeshkin and R. W. Boyd, *Phys. Rev. Lett.*, 2004, **92**, 083903–083914.
63 J. D. Rancourt, *Optical Thin Films: User Handbook*, SPIE, Bellingham, WA, 1996.
64 J. S. Foresi, P. R. Villeneuve, J. Ferrera, E. R. Thoen, G. Steinmeyer, S. Fan, J. D. Joannopoulos, L. C. Kimerling, H. I. Smith and E. P. Ippen, *Nature*, 1997, **390**, 143.
65 J. P. Dowling, *Science*, 1998, **282**, 1841.
66 O. Painter, R. K. Lee, A. Scherer, A. Yariv, J. D. O'Brien, P. D. Dapkus and I. Kim, *Science*, 1999, **284**, 1819.
67 A. Yadav, A. Kaushik, Y. K. Mishra, V. Agrawal, A. Ahmadivand, K. Maliutina, Y. Liu, Z. Ouyang, W. Dong and G. J. Cheng, *Mater. Today Chem.*, 2020, **15**, 100208.
68 M. Madou, *Fundamentals of Microfabrication*, CRC Press, New York, 1997.
69 (*a*) S. Y. Lin, J. G. Fleming, D. L. Hetherington, B. K. Smith, R. Biswas, K. M. Ho, M. M. Sigalas, W. Zubrzycki, S. R. Kurtz and J. Bur, *Nature*, 1998, **394**, 251; (*b*) J. G. Flemming and S.-Y. Lin, *Opt. Lett.*, 1999, **24**, 49.
70 (*a*) S. Noda, N. Yamamoto and A. Sasaki, *Jpn. J. Appl. Phys.*, 1996, **35**, L909; (*b*) S. Noda, K. Tomoda, N. Yamamoto and A. Chutinan, *Science*, 2000, **289**, 604.
71 M. C. Wanke, O. Lehmann, K. Muller, Q. Wen and M. Stuke, *Science*, 1997, **275**, 1284.
72 B. H. Cumpston, S. P. Anathavel, S. Barlow, D. L. Dyer, J. E. Ehrlich, L. L. Erskine, A. A. Heikal, S. M. Kuebler, I. Y. S. Lee, D. McCord-Maughon, J. Q. Qin, H. Rockel, M. Rumi, X. L. Wu, S. R. Marder and J. W. Perry, *Nature*, 1999, **398**, 51.
73 M. Campbell, D. N. Sharp, M. T. Harrison, R. G. Denning and A. J. Turberfield, *Nature*, 2000, **404**, 53.
74 B. Gates, S. H. Park and Y. Xia, *J. Lightwave Technol.*, 1999, **17**, 1956.
75 R. J. Hunter. *Foundations of Colloid Science*, Oxford University Press, Oxford, 1989.
76 N. D. Denkov, O. D. Velev, P. A. Kralchevsky, I. B. Ivanov, H. Yoshimura and K. Nagayama, *Langmuir*, 1992, **8**, 3183–3190.
77 N. D. Denkov, O. D. Velev, P. A. Kralchevsky, I. B. Ivanov, H. Yoshimura and K. Nagayama, *Nature*, 1993, **361**, 26.
78 Y.-W. Chung, I.-C. Leu, J.-H. Lee and M.-H. Hon, *Langmuir*, 2006, **22**, 6454–6460.
79 K. W. Tan, Y. K. Koh, Y.-M. Chiang and C. C. Wong, *Langmuir*, 2010, **26**, 7093–7710.

80 S. Wong, V. Kitaev and G. Ozin, *J. Am. Chem. Soc.*, 2003, **125**, 15589–15598.
81 N. V. Dziomkina and G. J. Vancso, *Soft Matter*, 2005, **1**, 265–279.
82 T. Ding, K. Song, K. Clays and C. H. Tung, *Adv. Mater.*, 2009, **21**, 1936–1940.
83 Q. Yan, L. Gao, V. Sharma, Y.-M. Chiang and C. C. Wong, *Langmuir*, 2008, **24**, 11518–11522.
84 P. Jiang, J. F. Bertone, K. S. Hwang and V. L. Colvin, *Chem. Mater.*, 1999, **11**, 2132–2140.
85 Q. Yan, *et al.*, Inward-Growing Self-Assembly of Colloidal Crystal Films on Horizontal Substrates, *Langmuir*, 2005, **21**(7), 3158–3164.
86 (*a*) J. M. Lehn, *Angew Chem. Int. Ed. Engl.*, 1990, **29**, 1304; (*b*) G. M. Whitesides, *Sci. Am.*, 1995, **273**, 146.
87 A. Yadav, *et al.*, The spectral plasmonic effect in the nano-cavity of dye-doped nanosphere-based photonic crystals, *Nanotechnology*, 2016, **27**, 165703.
88 A. Yadav, *et al.*, Spectral properties of self-assembled polystyrene nanospheres photonic crystals doped with luminescent dyes, *Opt. Mater.*, 2013, **35**(8), 1538–1543.
89 R. De Angelis, *et al.*, From nanospheres to microribbons: self-assembled Eosin Y doped PMMA nanoparticles as photonic crystals, *J. Colloid Interface Sci.*, 2014, **414**, 24–32.
90 D. Philp and J. F. Stoddart, *Angew Chem. Int. Ed. Engl.*, 1996, **35**, 1154.
91 Y. Xia, B. Gates and Z.-Y. Li, *Adv. Mater.*, 2001, **13**, 409–413.
92 P. Jiang, *et al.*, *Chem. Mater.*, 1999, **11**, 2132–2140.
93 S. Furumi, H. Fudouzi and T. Sawada, *Laser Photon. Rev.*, 2010, **4**, 205–220.
94 M. L. Garcìa, Self-Assembled Photonic-Plasmonic Crystals for Light control at the Nanoscale, *Ph. D. thesis*, ICMM. Photonic Crystals Group, 2011.
95 M. H. Kim, H. K. Choi, O. O. Park and S. H. Im, *Appl. Phys. Lett.*, 2006, **88**, 143127–3.
96 A. Yadav, *et al.*, Controlled Self-Assembly of Plasmon-Based Photonic Nanocrystals for High-Performance Photonic technologies, *Nano Today*, 2021, **37**, 101072.
97 A. Yadav, *et al.*, State-of-the-art plasmonic photonic crystal based on self-assembled nanostructures, *J. Mater. Chem. C*, 2021, **9**, 3368–3383.
98 H. Yang and P. Jiang, *Langmuir*, 2010, **26**, 13173–13182.
99 D. J. Norris, E. G. Arlinghaus, L. L. Meng, R. Heiny and L. E. Scriven, *Adv. Mater.*, 2004, **16**, 1393–1399.
100 A. Yadav, *et al.*, Fabrication of Self-Assembled Three-Dimensional Nano-Photonic Crystals and Potential Applications, *Sci. Adv. Today*, 2017, **3**, 25275.
101 A. Yadav, *et al.*, Fabrication of 3D polymeric photonic arrays and related applications, *Mater. Today Chem.*, 2020, **15**, 100208.
102 J. M. Meijer, F. Hagemans, L. Rossi, D. V. Byelov, S. I. R. Castillo, A. Snigirev, I. Snigireva, A. P. Philipse and A. V. Petukhov, *Langmuir*, 2012, **28**(20), 7631–7638.
103 Y. Xia, Y. D. Yin, Y. Lu and J. Mc Lellan, *Adv. Funct. Mater.*, 2003, **13**, 907–918.
104 A. Stein, F. Li and N. R. Denny, *Chem. Mater.*, 2008, **20**, 649–656.
105 J. Zhang, H. Liu, P. Zhan, Z. Wang and N. Ming, *Adv. Funct. Mater.*, 2007, **17**, 1558–1566.
106 Z. Zheng, X. Z. Liu, Y. H. Luo and B. Y. Cheng, *Appl. Phys. Lett.*, 2007, **90**, 051910.
107 H. Li and F. Marlow, *Chem. Mater.*, 2006, **18**, 1803–1810.
108 Y. Chung, I. C. Leu, J. H. Lee and M. H. Hon, *Langmuir*, 2006, **22**, 6454–6460.
109 M. Kim, S. H. Im and O. O. Park, *Adv. Funct. Mater.*, 2005, **15**, 1329–1335.
110 S. Furumi, H. Fudouzi, H. T. Miyazaki and Y. Sakka, *Adv. Mater.*, 2007, **19**, 2067–2072.
111 A. Yadav, *et al.*, Tunable random lasing behavior in plasmonic nanostructures, *Nanoconvergance*, 2017, **4**, 1.
112 Q. Zhang, *et al.*, Study of the impact of photonic crystals additives on the piezoresponse of PVDF nanofibers, *Nanoscale Adv.*, 2025, **7**, 4721–4729.
113 Y. Q. Zhang, J. X. Wang, Z. Y. Ji, W. P. Hu, L. Jiang, Y. L. Song, *et al.*, *J. Mater. Chem.*, 2007, **17**, 90–94.
114 J. W. Lee, J. Lee, C. Kim, C.-Y. Cho and J. H. Moon, *Sci. Rep.*, 2014, **4**, 1–7.
115 A. Mihi, C. Zhang and P. V. Braun, *Angew. Chem., Int. Ed.*, 2011, **50**, 5712–5715.
116 J.-H. Shin, J.-H. Kang, W.-M. Jin, J. H. Park, Y.-S. Cho and J. H. Moon, *Langmuir*, 2011, **27**, 856–860.
117 B. Mandlmeier, J. M. Szeifert, D. Fattakhova-Rohlfing, H. Amenitsch and T. Bein, *J. Am. Chem. Soc.*, 2011, **133**, 17274–17282.
118 P. R. Somani, C. Dionigi, M. Murgia, D. Palles, P. Nozar and G. Ruani, *Sol. Energy Mater. Sol. Cell.*, 2005, **87**, 513–519.
119 S.-H. A. Lee, N. M. Abrams, P. G. Hoertz, G. D. Barber, L. I. Halaoui and T. E. Mallouk, *J. Phys. Chem. B*, 2008, **112**, 14415–14421.
120 Y. G. Seo, K. Woo, J. Kim, H. Lee and W. Lee, *Adv. Funct. Mater.*, 2011, **21**, 3094–3103.
121 B. O'Regan and M. Grätzel, A low-cost, high-efficiency solar cell based on dye-sensitized colloidal TiO2 films, *Nature*, 1991, **353**, 737–740.
122 A. Mihi and H. Míguez, *J. Phys. Chem. B*, 2005, **109**, 15968–15976.
123 A. Mihi, F. J. López-Alcaraz and H. Míguez, *Appl. Phys. Lett.*, 2006, **88**, 193110.
124 Y. Zhang, J. Wang, Y. Zhao, J. Zhai, L. Jiang, Y. Song and D. Zhu, *J. Mater. Chem.*, 2008, **18**, 2650.
125 H. M. An, J. I. Sim, K. S. Shin, Y. M. Sung and T. G. Kim, *IEEE J. Quantum Electron.*, 2012, **48**, 891–896.
126 K. H. Li, K. Y. Zang, S. J. Chua and H. W. Choi, *Appl. Phys. Lett.*, 2013, **102**, 1–5.
127 Q. Lin, S. Liang, J. Wang, R. Zhang and X. Wang, *Inorg. Chem.*, 2022, **61**, 2920–2928.
128 X. Ning, Y. Wu, X. Ma, Z. Zhang, R. Gao, J. Chen, D. Shan and X. Lu, *Adv. Funct. Mater.*, 2019, **29**, 1902992.
129 J. Jasieniak, B. I. MacDonald, S. E. Watkins and P. Mulvaney, *Nano Lett.*, 2011, **11**, 2856–2864.
130 Y. Wang, H. Arandiyan, J. Scott, A. Bagheri, H. Dai and R. Amal, *J. Mater. Chem. A*, 2017, **5**, 8825–8846.

131 H. Wu, R. Irani, K. Zhang, L. Jing, H. Dai, H. Y. Chung, F. F. Abdi and Y. H. Ng, *ACS Energy Lett.*, 2021, **6**, 3400–3407.
132 X. Zheng, G. Shen, C. Wang, Y. Li, D. Dunphy, T. Hasan, C. J. Brinker and B.-L. Su, *Nat. Commun.*, 2017, **8**, 14921.
133 Y. Lu, H. Zhang, D. Fan, Z. Chen and X. Yang, *J. Hazard Mater.*, 2022, **423**, 127128.
134 F. Wen and W. Liu, *J. Mater. Chem. A*, 2021, **9**, 18129–18147.
135 P. Gao, A. Hunter, S. Benavides, M. J. Summe, F. Gao and W. A. Phillip, *ACS Appl. Mater. Interfaces*, 2016, **8**(5), 3386.
136 P. Gao, A. Hunter, M. J. Summe and W. A. Phillip, *ACS Appl. Mater. Interfaces*, 2016, **8**(30), 19772.
137 S. J. Lee, D. N. Heo, M. Heo, M. H. Noh, D. Lee, S. A. Park, J.-H. Moon and I. K. Kwon, *J. Ind. Eng. Chem.*, 2017, **46**, 273.
138 R. Bernstein, C. E. Singer, S. P. Singh, C. Mao and C. J. Arnusch, *J. Membr. Sci.*, 2018, **548**, 73.
139 A. B. Alayande, S. Chae and I. S. Kim, *Sep. Purif. Technol.*, 2019, **226**, 68.
140 A. B. Alayande, H.-D. Park, J. S. Vrouwenvelder and I. S. Kim, *Small*, 2019, **15**(28), 1901023.
141 E. Y. M. Ang, T. Y. Ng, J. Yeo, R. Lin, Z. Liu and K. R. Geethalakshmi, *Phys. Chem. Chem. Phys.*, 2018, **20**(20), 13896.
142 A. Gogoi, T. J. Konch, K. Raidongia and K. A. Reddy, *J. Membr. Sci.*, 2018, **563**, 785–793.
143 R. K. Joshi, S. Alwarappan, M. Yoshimura, V. Sahajwalla and Y. Nishina, *Appl. Mater. Today*, 2015, **1**(1), 1.
144 B. Liang, W. Zhan, G. Qi, S. Lin, Q. Nan, Y. Liu, B. Cao and K. Pan, *J. Mater. Chem. A*, 2015, **3**(9), 5140.
145 B. Mi, *Science*, 2014, **343**(6172), 740.
146 X.-F. Sun, J. Qin, P.-F. Xia, B.-B. Guo, C.-M. Yang, C. Song and S.-G. Wang, *Chem. Eng. J.*, 2015, **281**, 53.
147 K. H. Thebo, X. Qian, Q. Zhang, L. Chen, H.-M. Cheng and W. Ren, *Nat. Commun.*, 2018, **9**(1), 1486.
148 M. Fathizadeh, H. N. Tien, K. Khivantsev, J.-T. Chen and M. Yu, *J. Mater. Chem. A*, 2017, **5**(39), 20860.
149 D. E. Rumelhart, G. E. Hinton and R. J. Williams, Learning representations by back-propagating errors, *Nature*, 1986, **323**, 533–536.
150 S. Lawrence, C. L. Giles, A. C. Tsoi, *et al.*, Face recognition: a convolutional neural- network approach, *IEEE Trans. Neural Network.*, 1997, **8**, 98–113.
151 K. Simonyan and A. Zisserman, Intense convolutional networks for large-scale image recognition, 2014, preprint, arXiv:1409.1566[cs.CV], DOI: **10.48550/arXiv.1409.1556**.
152 T. Ma, *et al.*, Review Optical multilayer thin film structure inverse design: from optimization to deep learning, *iScience*, 2025, **28**, 112222.
153 W. Yang, *et al.*, Spatiotemporal Programmability of 3D Chiral Color Units Driven by Ink Spontaneous Diffusion toward Customized Printing, *Adv. Mater.*, 2025, **37**(4), 2570031.